POLITECNICO DI TORINO

Master's Degree in Aerospace Engineering

Politecnico di Torino

Master's Degree Thesis

Particle-In-Cell Simulation Of Heavy Species In Hall Thruster Discharge

Supervisor

Prof. Lorenzo CASALINO

Co-Supervisors

Dr. Ing. Mario PANELLI

Dr. Ing. Francesco BATTISTA

Candidate

Antonio PETRONELLI

06/2021

POLITECNICO DI TORINO

Master's Degree in Aerospace Engineering

Politecnico di Torino

Master's Degree Thesis

Particle-In-Cell Simulation Of Heavy Species In Hall Thruster Discharge

Supervisor

Prof. Lorenzo CASALINO

Co-Supervisors

Dr. Ing. Mario PANELLI

Dr. Ing. Francesco BATTISTA

Candidate

Antonio PETRONELLI

06/2021

Summary

Hall Effect Thrusters (HETs) are used for satellites applications, particularly orbiting at Low/Geo Earth Orbit (LEO/GEO) for telecommunications and government spacecraft because of their efficiency and competitiveness if compared to other electric propulsion devices. Furthermore, HETs have great potential because, in the future, they could be used for orbit transfers and interplanetary space missions. Computational modelling of plasma in HET has resulted interesting for several reasons. First, it can be used to predict thrusters' operative life; this feature, indeed, is compromised by the contact of plasma particles with the walls of the device (erosion phenomenon). Secondly, it can help to understand better the physic of these devices; the electron transport across the magnetic field and its coupling with the electric field and the neutral atom density are the phenomena that make complex and non-linear physics. Lastly, it can be used as a design tool for the next generation of thrusters. The behaviour of plasma heavy particles, namely neutrals and ions, has been analysed by means of axisymmetric Particle-In-Cell (PIC) code (kinetic model), developed to be coupled with a module solving fluid equations (fluid model) for electrons (i.e. hybrid approach for plasma). In this work, only the PIC module has been developed. The discharge within the accelerating channel of the SPT-100 thruster has been selected as cornerstone test because of the great availability of numerical and experimental data. The study has shown that the code was able to describe accurately the density and velocity of ions and neutrals, reproducing with consistency the physics within the accelerating channel of HETs.

Table of Contents

List of Tables

List of Figures

Acronyms

BC
Boundary Conditions

CEX
Charge Exchange

CIRA
Italian Aerospace Research Centre

EDF
Energy Distribution Function

EP
Electric Propulsion

GEO
Geostationary Earth Orbit

HET(s)
Hall Effect Thruster(s)

JPL
Jet Propulsion Laboratory

MCC
Monte Carlo Collision

MPD
Magnetoplasmadynamic Thruster

PIC

Particle In Cell

PPT

Pulsed Plasma Thruster

PPU

Power Processor Unit

RHS

Right Hand Side

SPT

Stationary Plasma Thruster

VDF

Velocity Distribution Function

Chapter 1

Introduction

1.1 Electric Propulsion History

Electric propulsion was first studied by Robert Goddard in 1906 who accelerated a working fluid, through electric power, producing thrust. During the 1960s, the USA and Russia started significant electric propulsion research programs to develop this technology for satellite station-keeping and deep-space propulsion applications [1].

In the past 30 years, how shown in Fig. 1.1, electrical propulsion use in spacecraft has grown worldwide and it is an advantageous alternative to chemical thruster for station-keeping applications in GEO communication satellites. Electric propulsion, indeed, allows reducing the propellant mass for station-keeping and orbit insertion compared to conventional chemical propulsion systems. For example, in 2014, SPT-100 Hall thrusters (reference thruster in this thesis) were used aboard the Express-AM5 and Express-AM6 satellites to perform an orbit-raising maneuver to reach their final orbit [2].

Regarding future uses, HETs have great potential because they could be used for orbit transfers and interplanetary space missions [3].

1.2 Physics Principles

The main advantage of electric propulsion is the high exhaust velocity of the working fluid that allows obtaining a more efficient use of propellant to have an increase of payload fraction. This means that an electric thruster achieves a high value of specific impulse, defined as:

$$I_{sp} = \frac{u_e}{g} \tag{1.1}$$

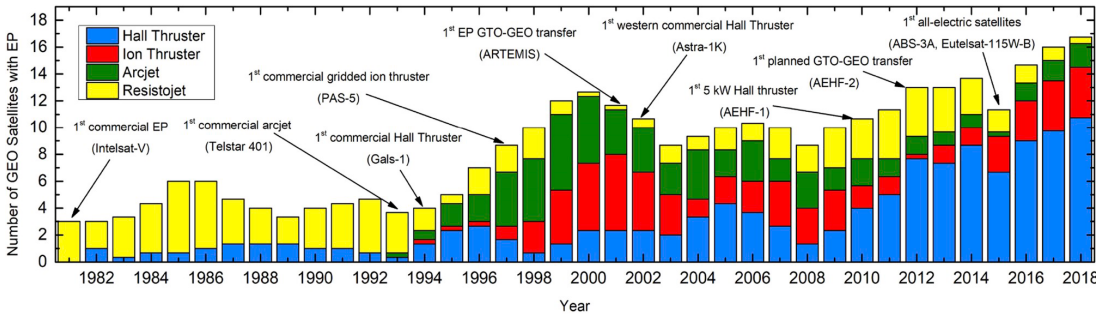

Figure 1.1: Number of EP-based GEO satellites launched in the years 1981–2018, divided into electric thruster subclasses [2].

where u_e is exhaust velocity and g is the gravitational acceleration. This characteristic supplies greater efficiency than other thrusters. Table 1.1 shows the specific impulse of the main thruster.

Thruster	**Specific Impulse [s]**
Cold gas	50/75
Chemical (monopropellant)	150/225
Chemical (bipropellant)	300/450
Resistojet	300
Arcjet	500/600
Ion thruster	2500/3600
Hall thruster	1500/2000
PPT	850/1200

Table 1.1: Typical specific impulse for different thrusters [1].

It is possible to prove it through the third law of dynamics for a spacecraft (assuming negligible the gravitational force and the aerodynamic drag):

$$m\dot{v} = \dot{m}u_e \tag{1.2}$$

where m and $\dot{v}$ are the mass and acceleration of spacecraft, $\dot{m}$ is the mass flow rate and u_e is the exhaust velocity. The thrust appears in the equation, defined as:

$$T = \dot{m}u_e \tag{1.3}$$

The integration of the thrust over the total time during which the propulsion is provided defines the total impulse:

$$I = \int T dt \tag{1.4}$$

It is possible to note that for a certain total impulse I, a high exhaust velocity ue leads to a minor usage of propellant.

Finally, integrating Eq. 1.2 it is possible to obtain:

$$\Delta v = u_e \ln \frac{m_0}{m_f} \tag{1.5}$$

where Δv is the total increment of the velocity of spacecraft, m_0 is the initial mass of spacecraft and m_f is the final mass of spacecraft and includes the mass of the rocket, casing, engine, tank, and payload.

Δv represents a feasibility index for the mission. The Tab. 1.2 shows typical Δv for various missions.

Mission	Δv, $\frac{m}{s}$
Escape from Earth surface (impulsive)	1.12×10^4
Escape from 480 km orbit (impulsive)	3.15×10^3
Escape from 480 km orbit (gentle spiral)	7.59×10^3
Earth orbit to Mars orbit and return*	1.4×10^4
Earth surface to Mars surface and return*	3.4×10^4
Earth orbit to Venus orbit and return*	1.6×10^4
Earth orbit to Mercury orbit and return*	3.1×10^4
Earth orbit to Jupiter orbit and return*	6.4×10^4
Earth orbit to Saturn orbit and return*	1.1×10^5

Table 1.2: Characteristic velocity increments for planetary transfer missions (*Hohmann's maneuver) [4].

It is possible to rewrite Eq. 1.5 as the fraction of mass that can be accelerated with a Δv:

$$\frac{m_f}{m_0} = e^{-\frac{\Delta v}{u_e}} \tag{1.6}$$

It is clear, from this expression, that by increasing the exhaust velocity ue it is possible to increase the payload fraction (keeping constant the mass of propellant) or, replacing $m_f = m_0 - m_p$, where mp is the mass of propellant [4]:

$$\frac{m_p}{m_0} = 1 - e^{-\frac{\Delta v}{u_e}} \tag{1.7}$$

It is possible noting that by increasing the exhaust velocity ue the mass propellant fraction decreases. Because of these characteristics, the electric propulsion systems cannot be used as launchers but can be used for satellites attitude control, orbital correction, orbital transfer, and interplanetary mission.

These differences, compared to chemical propulsion, are mainly due to different storage methods of energy: in chemical thrusters, energy is stored into working fluids, in electric thrusters, indeed, there is a separate energy source. The separate energy source leads to an increase in mass.

It is possible to consider this aspect through the energy conversion efficiency of the thruster η and the specific mass of the power generation system α:

$$\eta = \frac{\dot{m} u_e^2}{2P} = \frac{u_e T}{2P} \tag{1.8}$$

$$\alpha = \frac{m_{pot}}{2P} \tag{1.9}$$

In η, the product between $\dot{m}$ and ue represent the propulsive power, while P is the electric power. In α, m_{pot} is the weight of power system.

From Eq. 1.8 and Eq. 1.9, it is possible to get an expression of m_{pot} as function of the specific impulse:

$$m_{pot} = \alpha P = \frac{\alpha T g_0 I_{sp}}{2\eta} \tag{1.10}$$

So, exists an optimal value of the specific impulse depending on α, η and t_m (mission time):

$$I_{sp} = \frac{1}{g_0}\sqrt{\frac{2\eta t_m}{\alpha}} \tag{1.11}$$

or

$$v_{opt} = \sqrt{\frac{2\eta t_m}{\alpha}} \tag{1.12}$$

So, there is an optimal value of exhaust velocity, or specific impulse, that maximizes the payload mass (Fig. 1.2) that depends on the power system, the thruster, and mission time [4].

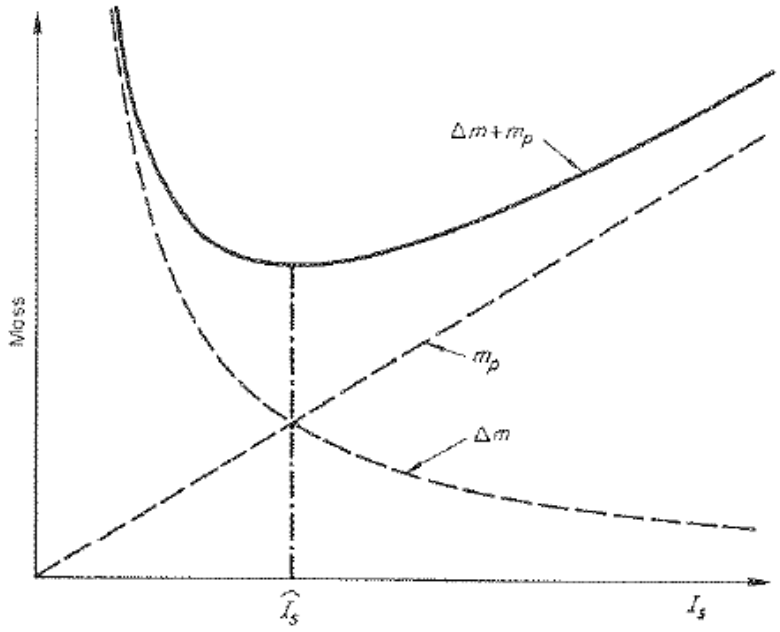

Figure 1.2: Optimal specific impulse: Δm is the propellant mass and m_p is the power supply mass [4].

1.2.1 Plasma Physics

Plasma is an "ionized" gas in which one or more electrons are torn from an atom, leaving a positive charge, called ion. This is achieved by injecting sufficient energy into the gas and it is considered the fourth state of matter.

Plasma is formed by a quasi-neutral mixture of charged and neutral particles with a chaotic motion. Because of the presence of free charges, Plasma is a good conductor where electrons move faster than ions, creating difference in potential.

Typically, it distinguishes between high temperature and low-temperature plasma, where temperature refers to the temperature of the electrons.

It is possible to define a distance (λ_D) for which for distances greater than λ_D electrons and ions can't move independently of each other because of the electric field generated from the splitting of atoms. For distances minor than λ_D, instead, the effects of individual charges predominate. This distance is called "*Debye length*" and can be calculated through the following equation:

$$\lambda_D = \sqrt{\frac{\epsilon_0 k_B T_e}{e^2 n}} \tag{1.13}$$

where ϵ_0 is the permittivity of free space, k_B is the Boltzmann constant, T_e is the

electron temperature, e is the charge of the electron and n is the charge density.

Nowadays plasma is used in numerous technologies in the industry, i.e. pixels of plasma TV, fluorescent light, packaging [5] [6].

1.3 Electric Thrusters' Classification

The electric thruster can be divided into three different categories: electrothermal, electrostatic, and electromagnetic. This division is made according to the mode of production of the thrust.

1.3.1 Electrothermal

In the electrothermal thruster, the propellant is heated by electric power and then is accelerated through a nozzle to produce thrust. Typically, electrothermal thrusters are resistojets and arcjets.

Resistojets heat the propellant with electric resistance. Arcjets bypass the limit of material of electrical resistance and deposit energy directly into the propellant using an electric arc.

The typical performance of these thrusters are specific impulse 300 s for 0.5-1.5 kW class hydrazine resistojet and a specific impulse 500-600 s for 0.3-2 kW class hydrazine arcojet.

1.3.2 Electrostatic

In the electrostatic thruster, a charged propellant is accelerated by the electrostatic field and at the exit of the thruster, the positive flow is neutralized by a negative particle beam. In this kind of thruster, the thrust density is constrained by space-charge limitations (Child-Langmuir law).

The typical performance of ion thruster are specific impulse 2800 s for 0.2-4 kW power. The typical performance of HET are specific impulse 1600 s for 0.3-6 kW power.

1.3.3 Electromagnetic

In the electromagnetic thruster is used a combination of electric (E) and magnetic (M) fields to accelerate a propellant and produce thrust.

Typically, electromagnetic thrusters are magnetoplasmadynamic thrusters (MPD) and pulsed plasma thruster (PPT). MPD thruster's performance are specific impulse 2000-5000 s for 1-100 kW power. The operating of PPT is like MPD but it operates in pulsed mode. PPT's performance are specific impulse 1000 s for 0.001-0.2 kW [7].

	Resistojet (N_2H_4)	**Arcjet Thruster** (N_2H_4)	**Ion** (X_e)	**HET** (X_e)	**MPD** applied field	**PPT** Teflon
Power range, W	500-1500	300-2000	200-4000	300-6000	1-100K	1-200
I_{sp}, s	300	500-600	2800	1600	2000-5000	1000
η	80%	35%	65%	50%	50%	7%
Peak Voltage	28	100	900	300	200	1K-2K
Thruster mass, kg/kW	1-2	0.7	3-6	2-3	-	120
PPU mass, kg/kW	1	2.5	6-10	6-10	-	110
Lifetime, h	500	>1000	10000	>7000	-	10^7pulse

Table 1.3: Typical parameters of electric thrusters.

1.4 Hall Effect Thruster

The Hall effect thruster (HET) is a hybrid between electrostatic and electromagnetic thrusters, indeed this kind of thruster uses a combination of electric (E) and magnetic (B) field to accelerate ionized propellant and to generate thrust. The geometry is cylindrical with an axially electric field and radial magnetic field. Fig. 1.3 shows a typical design of a HET.

The magnetic field is generated by coils, while the electric field is generated by potential difference created by cathode, external, and anode, inside the thruster. The magnetic field is minimum near the inlet section, while is maximum toward the exit, at coils. The potential, instead, is maximum near the inlet section, where there is a low electron density, while is minimum near the exit section, where the electron density increases. Fig. 1.4 shows this behaviour where B_r is the radial magnetic field and E_z is the axial electric field.

The external cathode generates a stream of electrons that moves toward the anode (because of its higher potential).

When the electrons enter the thruster, they get trapped in the zone of the max intensity of the magnetic field, so their motion to the anode is interrupted because of their small Larmor radius and their trajectory drifts in the azimuthal direction. In this way is created a Hall current. The ions, instead, are poorly affected. In

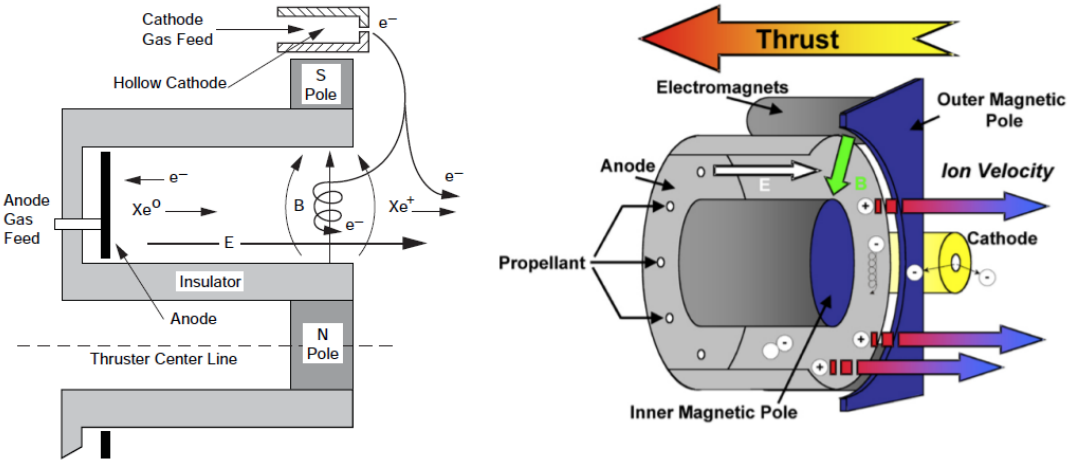

Figure 1.3: Hall Effect Thruster design [1] [8].

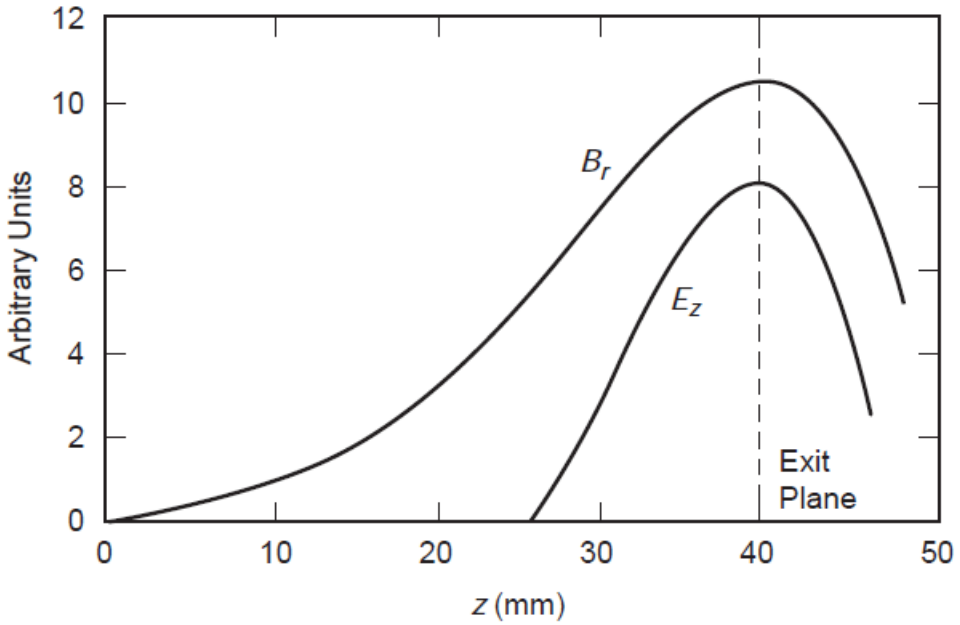

Figure 1.4: Axial electric field E_z and radial magnetic field B_r along the channel length [1].

particular the Larmor radius of electrons must satisfy:

$$r_{e,L} = \frac{v_{th}}{\omega_{c,e}} = \frac{m_e}{eB}\sqrt{\frac{8K_B T_e}{\pi m_e}} << L \tag{1.14}$$

here $r_{e,L}$ is the Larmour radius of electrons, v_{th} is the velocity of electrons due to their thermal motion, $\omega_{c,e}$ is the electron cyclotron frequency, m_e is the mass of electrons, K_B is the Boltzmann constant while L is the length of the acceleration channel.

On the contrary, the Larmour radius of ions has to be greater than the length of the channel:

$$r_{i,L} = \frac{v_i}{\omega_{c,i}} = \frac{1}{B}\sqrt{\frac{2M_i\phi}{e}} >> L \tag{1.15}$$

where $r_{i,L}$, v_i, $\omega_{c,i}$, M_i and ϕ are respectively the Larmour radius, the velocity, the cyclotron frequency and the mass of the ions, the net voltage through which the ion are accelerated, while B is the strength of the magnetic field. Only the electrons have to be magnetized, this mean that the square of the cyclotron frequency (ω_c^2) must be greater than the square of the total collision frequency (ν^2):

$$\Omega_e^2 = \frac{\omega_c^2}{\nu^2} \tag{1.16}$$

here Ω_e is the Hall parameter. Eq. 1.16 states that the electrons must travel for several orbits of their Larmour motion before a collision occurs.

The electrons undergo the magnetic force given from the following equation:

$$F_{Be} = qv_e \times B = qE = \frac{J_e}{n_e} \times B \tag{1.17}$$

where J_e is the current density, n_e is the number of electrons for volume unit.

While the average drift velocity of electrons is:

$$v_\theta = \frac{E \times B}{B^2} = \frac{E_z}{B_r} \tag{1.18}$$

where z is the axial direction and r is the radial direction [9].

The propellant is injected from the anode and is ionized by the collisions with high-energy electrons. The propellants used are noble gas, typically Xenon because of its characteristics as high atomic mass and low ionization potential. Since the Larmour radius of the ions is greater than channel length, ions motion is not influenced by the magnetic field and so they are accelerated by potential gradient and the exit velocity is given by:

$$v_i = \sqrt{\frac{2q_i\phi}{m_i}} \tag{1.19}$$

where q_i and m_i are charge and mass of ions and ϕ is the potential.

The working fluid inside the ionization chamber is a quasi-neutral plasma because the number of ions is about the same number of electrons. Because of this quasi-neutrality condition, there is no space charge limitation and so this type of thruster has not the limitation of thrust density imposed by Child law [10]. This is the first advantage of HET respect to other electric thrusters. The second advantage is the lower complexity of the device, due to two reasons: since ionization is mainly due to collisions between electrons and neutrals, there is no need for a device for ionization; moreover, the axial electric field is generated inside the plasma thanks the magnetic field, so there is no need for acceleration grid, as is shown in Fig. 1.5. The third advantage is the absence of the acceleration grid; indeed, this last has to be powered by PPU. So its absence save PPU mass (i.e. kg/kW). The fourth advantage is always about PPU mass saving; in HET it is possible to use the permanent magnets that do not need to be powered compared to the electro-induced ones. The last advantage is the possibility to scale up or down a baseline design [11].

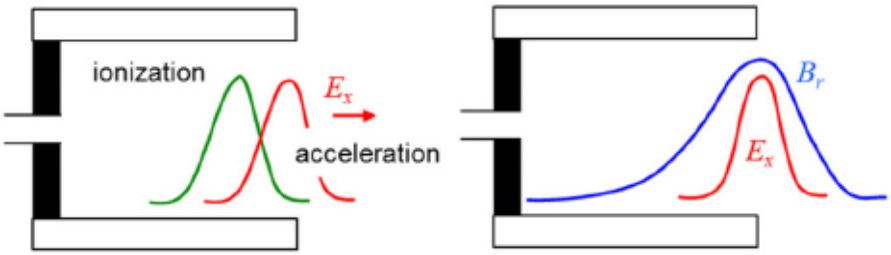

Figure 1.5: Schematic representation of the acceleration and ionization regions and of the radial magnetic field profile [12].

Conversely, the main limitation of HET is the low operative life, which depends on the erosion of the chamber's walls. Erosion is the gradual removal of material from the walls via plasma sputtering. Consequently, wall erosion exposes magnetic circuit components to plasma causing a reduction of performance and operative life [13].

1.4.1 Oscillations in Hall Effect Thrusters

HETs have the capability of generating many different waves and instabilities with frequencies from 1 kHz to tens of MHz [1]. The most observed oscillations, intrinsic to the physics of HETs, are associated with:

- ionization instabilities and rotational oscillations in the annular discharge channel;

- in azimuthal direction, can occur due to magnetic field gradient [14];
- axial motion of the ions through the ionization and acceleration regions.

In particular, the ionization instability is explained as depletion and replenishment of the neutrals near the exit section. Since the magnetic field in this region is large, the associated low electron conductivity leads to an increase in the electric field required to maintain current continuity. So ionization increases and depletes the neutral density causing moving back upstream of the neutral flow into a region where the ionization rate is lower. This effect causes a decrease in the flux of electrons to the exit, which causes the ionization there to abate and effectively brings back downstream the neutrals [15]. This kind of oscillation, which are typically observed in the discharge current, have been called "*breathing modes*" [16]. Anyway this aspect has not been analysed in this work thesis.

1.5 Plasma Modeling in Hall Effect Thruster

Computational modeling of plasma in HET has resulted interesting for several reasons. Firstly, it can be used to predict thrusters' operative life; this feature, indeed, is compromised by the contact of plasma particles with the walls of the device (*erosion phenomenon*). Secondly, it can help to understand better the physics of these devices; the electron transport across the magnetic field and its coupling with the electric field and the neutral atom density are the phenomena that make complex and non-linear physics. Lastly, it can be used as a tool to isolate physical effects, simplifying the understanding of the physics of these devices. So, these computational codes will also become useful design tools for the next generation of thrusters.

The main approaches to model HET plasma are fluid modeling, kinetic modeling, and hybrid modeling.

Fluid modeling [17] considers both electrons and heavy species (ions and neutrals) as a fluid and assume quasi-neutrality, or rather, the electrons number density is taken equal to the ions density ($n_e \simeq n_i$). It resolves the continuity equation, the momentum equation, and the energy equation. This approach is computationally efficient but the main drawback is the inability to model the velocity (VDF) and the energy distribution function (EDF).

Kinetic modeling [18] considers electrons and ions as discrete particles while neutrals can be modeled alternatively as a fluid or as particles. Each simulated particle is representative of a large number of real particles, and their trajectory is followed in the phase space considering both electric and magnetic fields. The discrete particles automatically model VDF and EDF but the computational cost for this approach is very high.

Hybrid modeling [19] offers a good compromise between fluid modeling and kinetic modeling. In this approach, ions are modeled as discrete particles and electrons are modeled as a fluid. Typically the geometry used are 1-D, 2-D radial-axial (r,z), and 2-D radial-azimuthal (r,θ). The advantages of this approach are to be able to capture non-Maxwellian features for the heavy species (so VDF and EDF) and having a computational cost between fluid and kinetic. The drawback is that this approach is not self-consistent: indeed, fluid approaches require modelling of electron transport across the magnetic streamlines that, as far as the author knows, actually depends on empirical parameters [12].

1.6 Motivation of the work and overview

The Italian Aerospace Research Centre (CIRA) in the framework of the activities on space electric propulsion (MEMS project) has started to develop an in-house hybrid plasma model called **HY**brid **PIC-FLU**id (from which the acronyms **HYPICFLU** [20]). The hybrid approach, as mentioned in the previous section, allows describing the VDF for the heavy species with a low computational cost.

HYPICFLU is formed by two different modules: the Particle-In-Cell (PIC) module for the heavy species (neutrals and ions), while the fluid model for electrons.

Particularly, the PIC module calculates the time variation of densities and velocities of neutrals and ions (n_i, n_n, v_i, v_n) be known the electron temperature and electric field. They can be arbitrarily assigned, or they can be otherwise computed using the fluid module.

The two modules communicate iteratively each other because the outputs of a module are the inputs of the other and vice-versa. Fig. 1.6 shows this iterative cycle where n_n, v_n, n_i, v_i are density and velocity of neutrals and ions, $\dot{n}_i$ is the ionization rate, B is magnetic field, T_e is electron temperature, Φ is electric potential, and E_z is electric field.

The purposes of this thesis work are the development and the validation of the HYPICFLU-PIC module. Moreover, an attempt was made to lay the foundations for the study of the erosion phenomenon in the thruster and so for predicting the operative life and the decrease of the performance.

Chapter 2 deals with the governing equations, the assumptions made for the particles, the description of the PIC model, and the main functions of the code. Chapter 3 shows the main test cases selected to validate the results of PIC module. SPT-100 thuster is selected as reference engine because the availability of experimental and numerical data (e.g. cf. [21, 22]). Particularly, HPHALL-2 code [21, 23] is selected for code-code comparison.

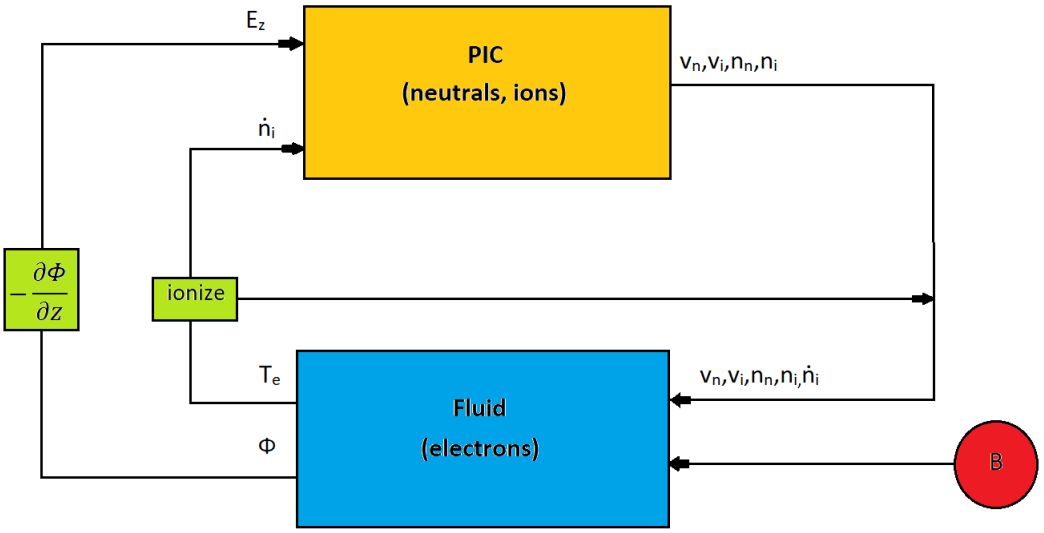

Figure 1.6: Hybrid model: interaction between PIC and Fluid modules. n_n, v_n, n_i, v_i are density and velocity of neutrals and ions, $\dot{n}_i$ is the ionization rate, B is magnetic field, T_e is electron temperature, Φ is electric potential, and E_z is electric field.

Chapter 2

Heavy Particles Simulation

Heavy Particles, i.e. ions and neutrals, are modeled with a PIC method. Each simulated particle represents an agglomerate of real particles, typically 10^8 to 10^{12} particles [20]. This method is used because a code that simulates each particle is non-feasible from the computational point of view. The "specific weight" represents the number of real particles in each macro-particles; it varies among the particles and changes over time. Each Macro-particle is tracked in the phase space.

2.1 Ions

The second law of Dynamic written for an ion is:

$$\vec{a} = \frac{q}{m}\left[\vec{E} + \vec{v} \times \vec{B}\right] \tag{2.1}$$

where a is the acceleration, q/m is the charge to mass ratio of the macroparticle, v is its velocity while $\vec{E}$ and $\vec{B}$ are respectively the electric and the magnetic field in the ion's position. Since the ions are not magnetized they are less sensitive to the magnetic field and the second term on the RHS can be neglected. Hence, the acceleration of each ion is:

$$\vec{a} = \frac{q}{m}\vec{E} \tag{2.2}$$

The precedent equation has to be integrated each time step to update the particle's velocity and position.

2.2 Neutrals

In the case of neutral particles, by considering that their mean free path is greater than the channel length, there is a simplification concerning the possibility of neglecting both neutral-neutral and ion-neutral collisions. Furthermore, neutral particles are not influenced by the electric or the magnetic field. Hence, a macro-neutral can change its velocity only if it collides with a wall.

2.3 Ionization

In the model herein presented, two simplifying assumptions are made: only electron-neutral collisions can produce ions and only singly-ionized atoms are considered. Particularly, the second assumption is important because double ionized ions can produce important effect on the performance, as in-homogeneous flow. However, the latter aspect has not been analysed in this work and it is saved for the future.

The ionization rate, $\dot{n_i}$, defined as the rate at which ions are created per unit volume, is expressed in the following formulation [19]:

$$\dot{n_i} = n_e n_n \zeta(T_e) \tag{2.3}$$

where $\dot{n_i}$ is the ionization rate, $\zeta(T_e)$ is the ionization coefficient while n_e and n_n are respectively the electron and the neutral number density.

$\zeta(T_e)$ is a function that only depends on the electron temperature and can be approximated, for the xenon atoms, as [1]:

$$\zeta(T_e) \simeq 10^{-20} \left[\left(3.97 + 0.643 T_{eV} - 0.0368 T_{eV}^2 \right) e^{-\frac{12.127}{T_{eV}}} \right] \left(\frac{8 e T_{eV}}{\pi m} \right)^{\frac{1}{2}} \tag{2.4}$$

$$\zeta(T_e) \simeq 10^{-20} \left[-1.31 \cdot 10^{-4} T_{eV}^2 + 6.386 e^{-\frac{12.127}{T_{eV}}} \right] \left(\frac{8 e T_{eV}}{\pi m} \right)^{\frac{1}{2}} \tag{2.5}$$

where Eq.2.4 is valid for $T_e < 5eV$ while Eq.2.5 for $T_e \geq 5eV$. Here T_{eV} is the electron temperature expressed in electron Volt, e is the elementary charge and m is the electron mass. Fig. 2.1 shows the plot of $\zeta(T_e)$.

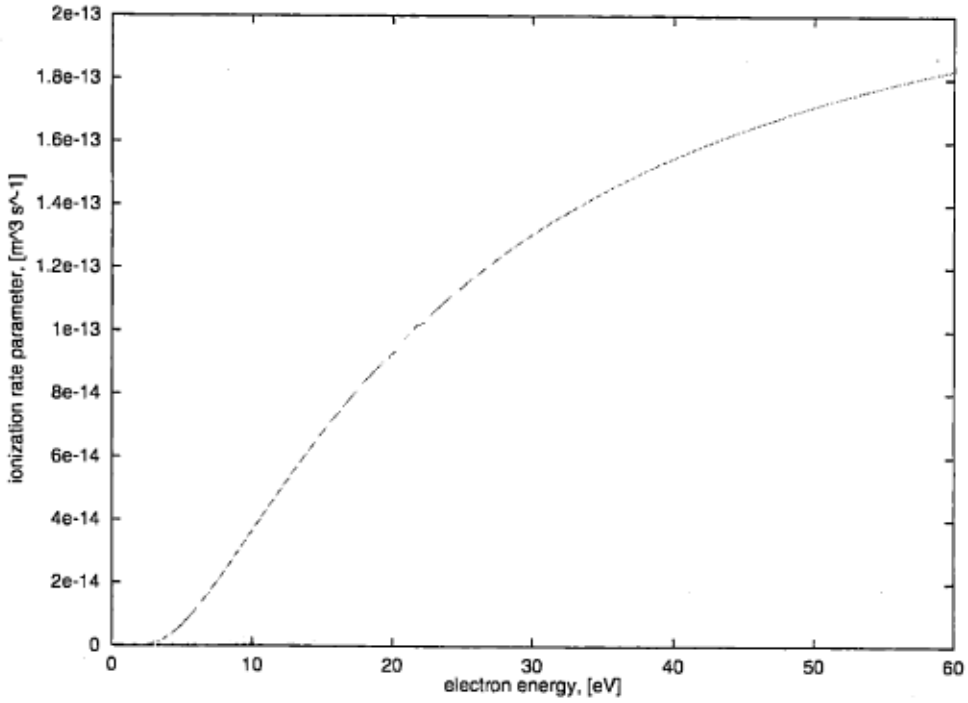

Figure 2.1: Ionization rate coefficient.

2.4 Charge Exchange and Bulk Recombination

The charge exchange (CEX) happens when an ion collides with a neutral and this collision produces a slow ion. The charge exchange cross-section for xenon (X_e and X_e^+), for typical velocities of SPT-100, is between $1 \cdot 10^{-18}$ m^2 and $4 \cdot 10^{-19}$ m^2. Near the anode, where the velocity of the ions is low and the neutral density is approximately 10^{20} m^{-3}, we obtain a mean free path of 1 cm that is comparable with the channel width and is smaller than channel length. In the plume, instead, due to the charge exchange, it may happen that ions are attracted into the thruster. Since the description of this phenomenon foresees the development of algorithms such as Monte Carlo Collision (MCC), that have a high computational cost, and since the effect in the thruster performance is limited the CEX has been neglected.

As shown in [19] the bulk recombination rate is many order of magnitude inferior to the bulk ionization rate, so the bulk recombination has been neglected.

2.5 Numerical Model

As mentioned in Par. 1.5, the hybrid modeling processes in different ways heavy particles and electrons: ions and neutrals are modeled as discrete particles and electrons are modeled as a fluid. This difference doesn't allow the use of a single grid and timescale for both models. In particular, in the heavy species module, the time instant between two successive iterations is set so that the distance traveled by a particle is no greater than the typical length of a cell, to guarantee numerical stability [19]. On the other hand, in fluid model, the timescale is set to guarantee the stability of the solution of the fluid solver. The fluid and the PIC module are integrated over the same time interval but with a different time-step e.g. the time-step of the fluid equations is about $10^{-11} \div 10^{-10} s$ while than of the PIC is $10^{-8} s$.

In an iteration of code, first the equation of motion for heavy species are integrated; the output of the PIC section are neutrals and ions density, their velocity and ionization rate. These outputs become input for the fluid section e remain constant during this phase. Finally, the outputs of the fluid section are electron temperature and electric potential (or electric field) that are used as input for the PIC section in the next iteration. Fig. 2.2 shows the typical operation of the hybrid model.

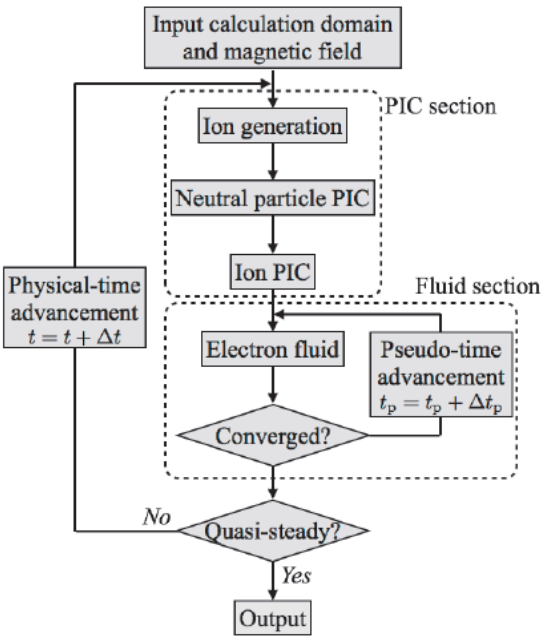

Figure 2.2: Flow-chart of typical hybrid model [24].

2.6 Particle-In-Cell Model

Heavy particles, i.e. neutrals and ions, are treated with the PIC model and are modeled as discrete particles. Each particle is characterized by position, velocity, specific weight, mass, charge, and logic coordinate. In order to calculate position and velocity, the equations of motion are integrated with the Leap-frog scheme (Eq. 2.17, 2.18). The time step, Δt, must ensure that the distance travelled by the particle is no greater than the typical length of the cell, so the maximum permissible value of Δt can be evaluated dividing the length of the cell by the maximum expected exhaust velocity. This ensures compliance with the Courant stability criterion ($\Delta t \leq \Delta x / v_{max}$).

The PIC module takes as input fixed value of electric and magnetic fields and electron temperature and estimated ions and neutrals properties and ionization rate. Fig. 2.3 shows a schematization of the PIC module and main functions.

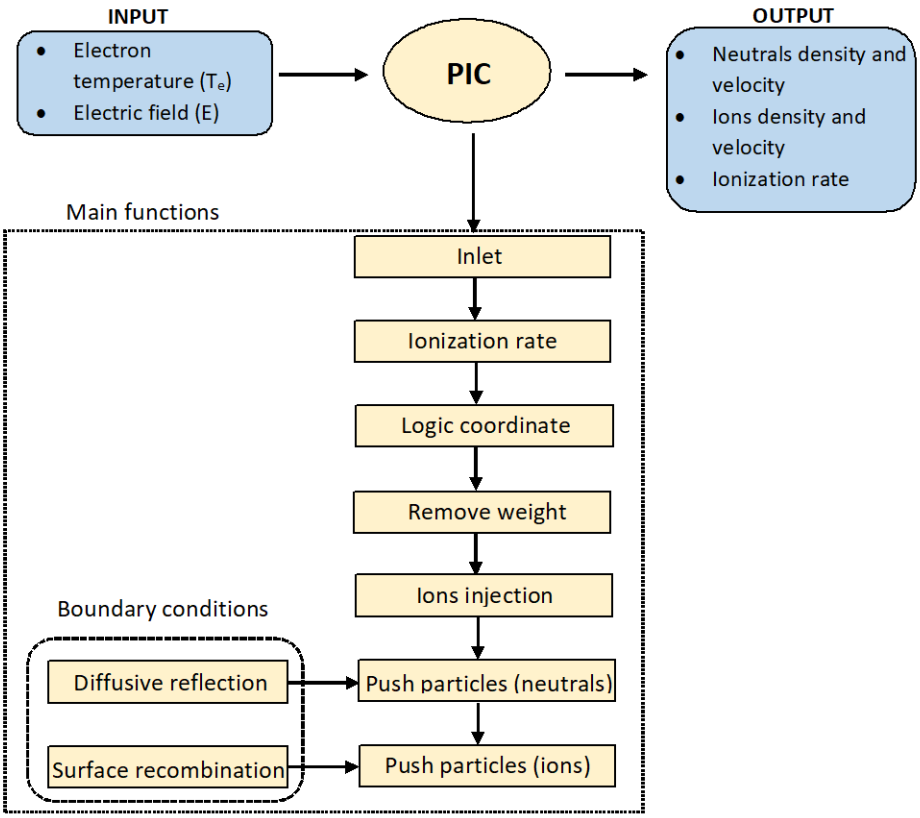

Figure 2.3: Schematization of PIC module.

In a standard PIC iteration neutrals enters into the domain through the anodic inlet, then the ionization rate is calculated using the input data. The data specified over the grid nodes (e.g. electron temperature and electric field) are interpolated to the position of each particle using a weighting function called *gather*. Afterward, neutrals are replaced with ions according to the ionization rate. Finally, the particles are advanced and the quantities associated with the particles are distributed to the grid nodes with another weighting function called *scatter*. So it is possible to evaluate neutrals density and velocity, ions density and velocity and ionization rate.

It should be noted that the functions for the injections of neutrals, diffusive reflection of neutrals, surface recombination of ions, the injections of ions are Monte Carlo based algorithms.

Numerical oscillations are expected because the PIC approach does not solve continuous equations while, physical oscillations (described in Par. 1.4.1) are not expected because, in this work, the PIC model is not coupled with the fluid model.

2.6.1 Computational Domain and PIC Mesh

The computational domain includes both the channel of the thruster and part of the near exit region (plume region), Fig. 2.4. The domain used in the previous version of the code [20] is a rectangle. The near-plume region has been extended in this work and it is modeled as a semicircular area the center of which is located on the channel axis and particularly at its exit. In order to analyse and simulate the behaviour of the plasma, symmetry with respect to the axis of the thruster was used, as shown in Fig. 2.4. The properties of the macroparticles simulated by the PIC module are interpolated on an elliptic mesh built within the domain (Fig. 2.4).

2.6.2 Weighting Functions: Gather and Scatter

The weighting functions are used in two distinct phases of the PIC module, in particular when the properties of the particles such as specific weight or velocity are distributed among the nodes of the cell where the particle is located and when the quantities defined over the nodes of the grid have to be interpolated to the particle's position. The first function is called scatter while the least is called gather and both the functions use a first-order algorithm.

Once the position of each particle is known the logical coordinates are retrieved: the integer part of these coordinates identifies the cell in which the particle is contained while the fractional part gives the position of the particle inside the cell. Finally, the fractional component of the logical coordinates is used by the weighting functions.

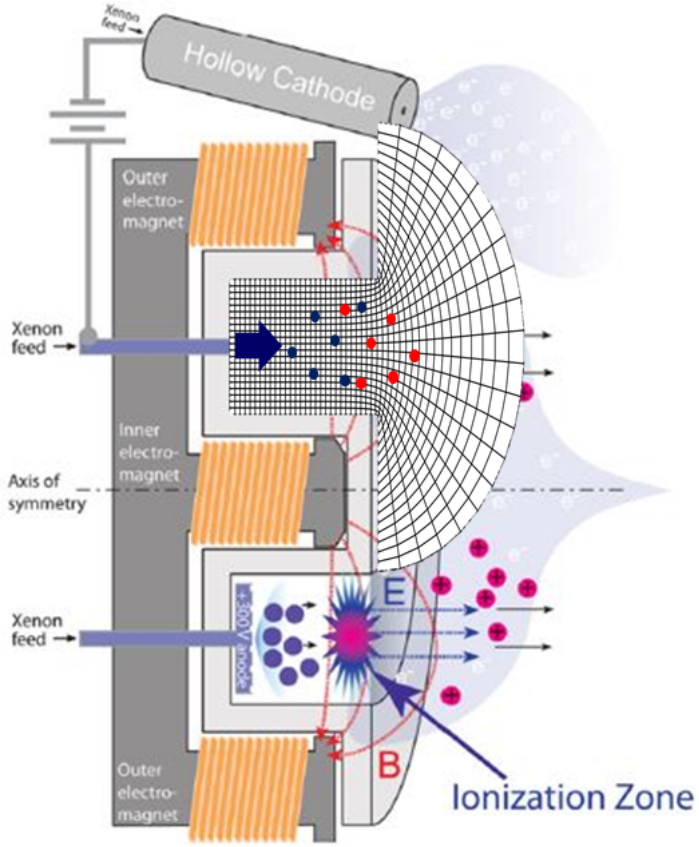

Figure 2.4: Section and symmetry of HETs. Computational domain and mesh for PIC approach.

The scatter algorithm can be written as:

$$f_1 = f_w(1 - \eta_{rel})(1 - \xi_{rel}) \tag{2.6}$$
$$f_2 = f_w\eta_{rel}(1 - \xi_{rel}) \tag{2.7}$$
$$f_3 = f_w\eta_{rel}\xi_{rel} \tag{2.8}$$
$$f_4 = f_w(1 - \xi_{rel})\eta_{rel} \tag{2.9}$$

where η_{rel} and ξ_{rel} are the fractional part of the logical coordinate of the particle, f_w is the quantity associated with the particle that has to be scattered while f_i is the fraction of this value associated to the i-th node of the cell, as shown in Fig. 2.5. Considering f_w as the specific weight, W_{sp}, the scatter allows to compute the number of particles for each node; dividing it by the volume associated to the nodes, V_{node} is possible to get the particles' density. Scattering the product of the specific weight and particle's velocity and dividing for the node volume and density

of the considered species, is possible to determine the nodal velocity.

The calculation of nodal volume, V_{node}, for elliptic mesh is more complicated than uniform mesh. In this work, it has been applied the procedure reported in [25].

The gather is the inverse of the scatter, calling f_w the values interpolated onto the particle position and f_i the quantity defined in the nodes of the cell:

$$f_w = f_1(1-\eta_{rel})(1-\xi_{rel}) + f_2\eta_{rel}(1-\xi_{rel}) + f_3\eta_{rel}\xi_{rel} + f_4(1-\xi_{rel})\eta_{rel} \quad (2.10)$$

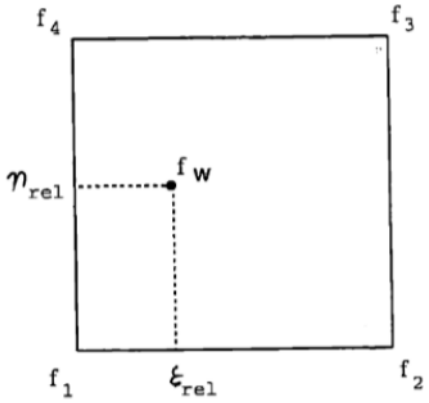

Figure 2.5: One dimensional weighting scheme for cartesian mesh [19].

Because the elliptic mesh is composed of arbitrary quadrilaterals, it is necessary to build a mapping function that transforms the real coordinate into logic and vice-versa, as shown in Fig. 2.6. The goal is to come up with a function such as $(x, y) = f(\xi, \eta)$ where $\xi \in [i, i+1]$ and $\eta \in [j, j+1]$ describe the entire point space enclosed by the quadrilateral. In addition $f(i, j) = (x_i, y_i)$, $f(i+1, j) = (x_{i+1}, y_i)$ and so on to correspond to the polygon vertices. This function, yet to be determined, forms a map that allows transforming the quad from the physical coordinate set to a logical coordinate space. In the logical coordinates, the polygon morphs into a square, regardless of its physical form. Once the logical coordinates are obtained, it is possible to perform the scatter and gather operations just as described above.

The following bi-linear mapping functions can be used:

$$x = \alpha_1 + \alpha_2\xi + \alpha_3\eta + \alpha_4\xi\eta \quad (2.11)$$

$$y = \beta_1 + \beta_2\xi + \beta_3\eta + \beta_4\xi\eta \quad (2.12)$$

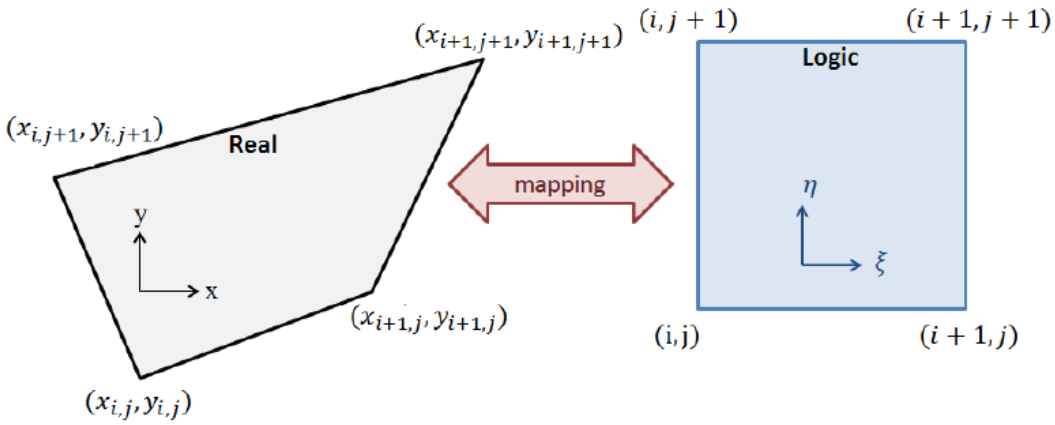

Figure 2.6: Real to logic coordinate mapping.

They can be written in matrix form:

$$\begin{bmatrix} x_{i,j} \\ x_{i+1,j} \\ x_{i+1,j+1} \\ x_{i,j+1} \end{bmatrix} = \underbrace{\begin{bmatrix} 1 & i & j & ij \\ 1 & i+1 & j & (i+1)j \\ 1 & i+1 & j+1 & (i+1)(j+1) \\ 1 & i & j+1 & i(j+1) \end{bmatrix}}_{A} \begin{bmatrix} \alpha_1 \\ \alpha_2 \\ \alpha_3 \\ \alpha_4 \end{bmatrix} \Longrightarrow \alpha_k = A^{-1}x \tag{2.13}$$

$$\begin{bmatrix} y_{i,j} \\ y_{i+1,j} \\ y_{i+1,j+1} \\ y_{i,j+1} \end{bmatrix} = A \begin{bmatrix} \beta_1 \\ \beta_2 \\ \beta_3 \\ \beta_4 \end{bmatrix} \Longrightarrow \beta_k = A^{-1}y \tag{2.14}$$

These expressions are solved for the coefficients α and β , easily by inverting the matrix A. Therefore for each cell there are 8 coefficients, α_k, β_k with $k = 1...4$. These can be computed once when the elliptic mesh has been defined and they can be stored as a lookup table.

2.6.3 Search-Locate Particles

To perform the weighting (or interpolation) step, the location of all the simulated particles (in real and logic spaces) must be known. The mapping function described in [26] and Allievi and Bermejo method [27] has been selected for the sake of simplifying the implementation.

The first step of the procedures is the research of the hosting cell, identified definitely by two integer numbers. In the second step, the fractional part of the logic coordinate is computed.

The algorithm is based on a different mapping function between real and logic coordinate (namely p and q).The transformed quadrilateral Ω is divided into four point convex quadrilaterals as shown in Fig. 2.7.

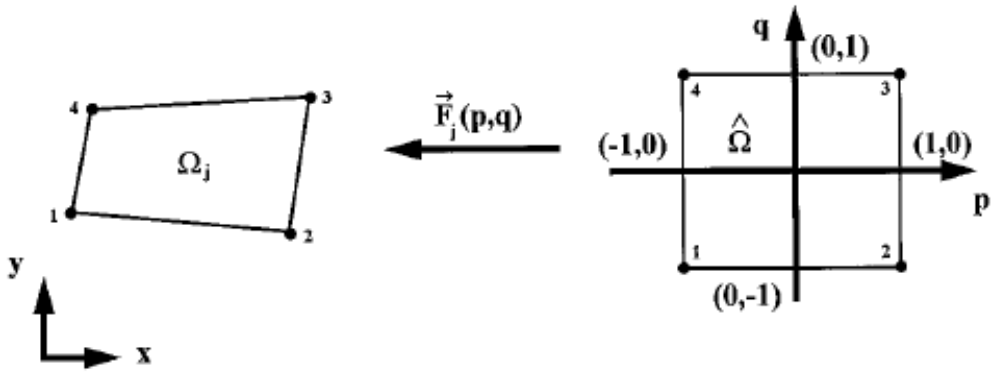

Figure 2.7: Mapping for bilinear quadrilateral elements [27].

2.6.4 Particles Advancer

The equation of motion of each particle can be written as:

$$\frac{\partial \vec{x}}{\partial t} = \vec{v_p} \tag{2.15}$$

$$\frac{\partial \vec{v}}{\partial t} = \vec{a_p} \tag{2.16}$$

where $\vec{a}$, the acceleration of the particle, is given by Eq. 2.2 for an ion while is zero for a neutral due to the assumption made in Sec. 2.2.

The equations of motion are valid in a cartesian reference system while some adjustments have to be made for an axial symmetrical geometry. Instead of using a set of cylindrical equations, a 3D cartesian set is used instead to simplify the implementation of the boundary conditions for the heavy species, after the particle is advanced in this fictitious space a rotation is performed to return the particle in the original plane [28].

The Eq. 2.15 and 2.16 are integrated using the leap-frog scheme (Fig. 2.8). The leap-frog algorithm integrates first the velocity and then updates the position of the particle. The velocity utilized to update the position has an offset of half of a time-step, this allows to obtain an integration scheme that is of order greater than

one, computationally fast and stable [29]. Denoting with k the time step and using the leap-frog scheme:

$$\vec{x}^{k+1} = \vec{x}^{k} + \vec{v_p}^{k+\frac{1}{2}}\Delta t \tag{2.17}$$

$$\vec{v_p}^{k+\frac{1}{2}} = \vec{v_p}^{k-\frac{1}{2}} + \frac{q}{m}\vec{E}\Delta t \tag{2.18}$$

This offset between the integration of position and velocity is created every time a new particle is injected in the domain, obtaining the acceleration in the instant when the particle is injected and integrating the velocity backward in time for half of a time step.

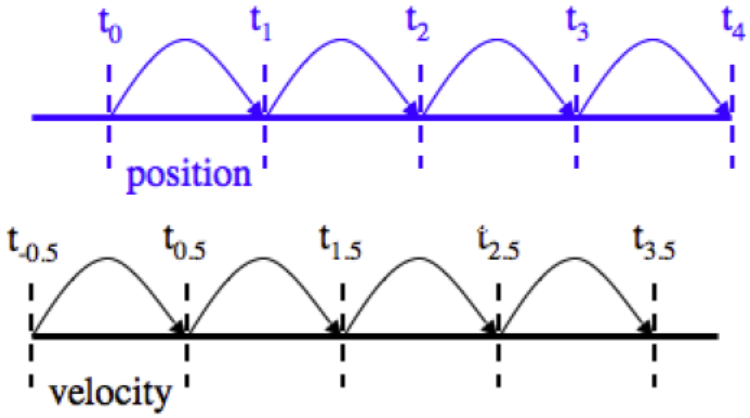

Figure 2.8: Leap-frog integration scheme [30].

2.6.5 Ionization

The ionization process is divided into two different steps: first, an integer number of macro ions are created in each cell according to the ionization rate defined over the nodes and then the mass is removed from each macro neutral in order to ensure the mass conservation. As shown in [31, 19] the number of macroions created in each cell is:

$$Nf_{i,cell} = \frac{m_i}{M_i}\dot{n}_{i,cell}V_{cell}\Delta t \tag{2.19}$$

where m_i is the mass of a xenon ion, M_i is the mass of a xenon macro-ion, Δt is the duration of a PIC interval, V_{cell} is the cell volume, and $\dot{n}_{i,cell}$ is the average ionization rate of the cell, i.e the ionization rate interpolated at the center of the

cell. $Nf_{i,cell}$ calculated above is a fractional number, the effective integer number of macro-ions created is calculated by applying a probabilistic algorithm on Eq. 2.19, in particular, a random number is generated and if this number is inferior to the fractional part of $N_{i,cell}$:

$$N_{i,cell} = int(Nf_{i,cell}) + 1 \tag{2.20}$$

here $int(Nf_{i,cell})$ is the integer component of Nf. After the ions are created in each cell, the mass has to be subtracted to each neutral in order to conserve mass, in particular, the mass variation of each neutral is:

$$\Delta M_n = (1 - n_e \eta(T_e) \Delta t) \cdot M_{n,o} \tag{2.21}$$

where ΔM_n is the mass subtracted to each macro-neutral while $M_{n,o}$ is the initial mass of the macro-neutral.

The position within the cell (at $t + \Delta t$) and the velocity (at $t + \Delta t/2$) of the generated macroions are selected randomly. For the velocity, a Maxwellian distribution, based on the most probable neutral velocity, based on the local fluid temperature of the neutrals (about 850K), is used. The leapfrog algorithm is applied to take into account which electric field acts on the new macroions at $t + \Delta t/2$ [31].

2.7 Boundary Conditions

Macro-neutrals are injected from the inlet, which is modeled as an annular ring located at the center of the anode wall. The velocities of the new-injected particles are calculated using a semi-Maxwellian distribution characterized by a set temperature.

Following Ref. [21] neutrals that collide with the walls are spread back into domain with a velocity sampled from a Maxwellian distribution at the wall temperature.

Regarding ions, it is assumed that each ion that collides with a wall recombines into a neutral (according to a pseudo-random condition so that the mass of neutrals created is comparable with the mass of ions destroyed), with a velocity that, again, is sampled from a semi-Maxwellian distribution at the wall temperature.

The particles that collide with the wall of channel generate the sputtering, a phenomenon that tend to increase the roughness of the walls and to decrease the operative life of thruster.

The particles that leave the domain outside of the channel are removed from the simulation.

The Fig. 2.9 shows a sketch of the Boundary Conditions (BC) applied to the PIC sub-module.

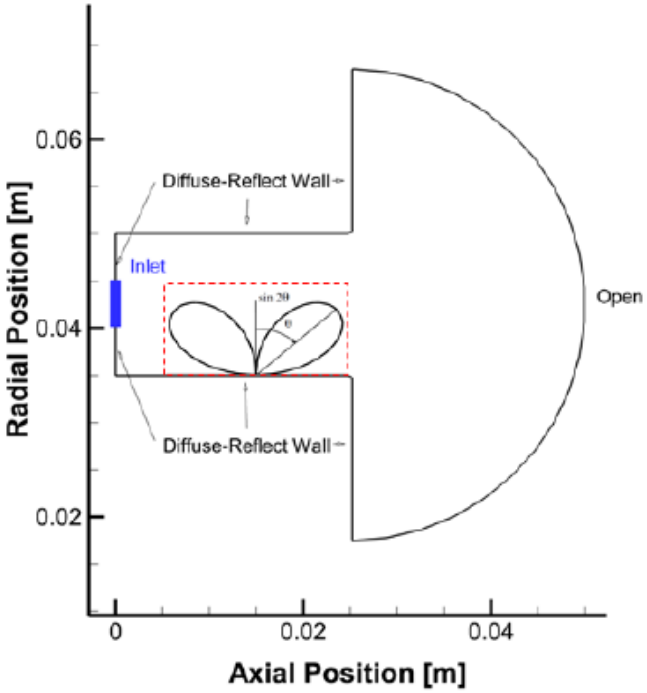

Figure 2.9: Boundary Conditions on the PIC sub-module.

Chapter 3

Simulation Results

This chapter describes and shows two test cases aimed to verify how the code is able to reproduce the typical physics within the accelerating channel of HETs. They are named neutral flux (plasma-off, i.e. only neutrals motion is present) and ion-neutral flux (plasma-on, i.e. both neutrals and ions motion are present) tests. A comparison of the simulations' results with numerical and experimental data will be presented. Moreover the assessment of the prediction capabilities of plasma properties by changing channel geometry (i.e. by considering eroded channel) will be investigated.

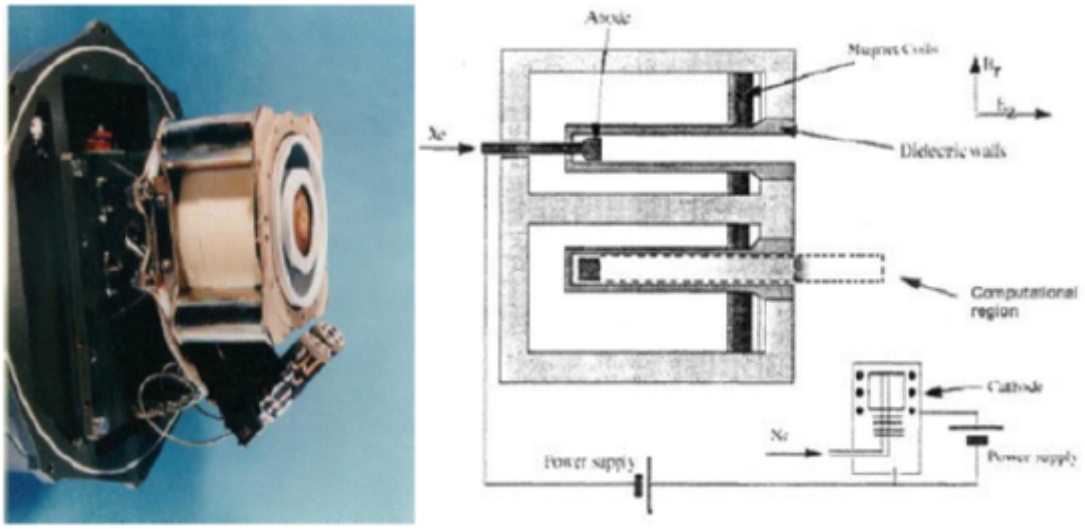

Figure 3.1: SPT-100 picture and sectional view.

3.1 Reference Thruster: SPT-100

SPT-100 is a HET manufactured by Russian EDB Fakel. It was first launched in 1994. In the following years, other versions of the SPT were developed and were used in many spacecraft such as IPSTAR-II, Telstar-8, and Ekspress. SPT stands for Stationary Plasma Thruster. Its operations are described in Par. 1.4 and the propellant used is Xenon. Fig. 3.1 shown a picture and a sectional view of SPT-100, while the main performance are shown in Tab. 3.1.

Parameters	**Value**
Propellant	Xenon
Power [W]	1350
Thrust [N]	0.08
Specific impulse [s]	1600
Efficiency	0.5
Lifetime	4000 hrs
No. of start-stop cycles	3000
Mass [kg]	4

Table 3.1: Main performance of SPT-100 [32].

SPT-100 has been chosen as the reference engine due to the large availability of data in literature [12, 21]. The main characteristics of the thruster are reported in Tab. 3.2.

Paramenters	**Values**
Channel length [m]	0.025
Channel width [m]	0.015
Inner radius [m]	0.035
Inner radius inlet [m]	0.04
External radius [m]	0.05
External radius inlet [m]	0.045
Mass flow rate [kg/s]	$5 \cdot 10^{-6}$
Discharge voltage [V]	300

Table 3.2: SPT-100 channel dimensions and nominal operating conditions parameters.

3.2 Neutral Flux

The neutral flow test case allows reproducing of the typical expansion of neutrals within the accelerating channel. Macro-neutrals are injected from the inlet, that is modeled as an annular ring positioned at the center of the anode wall. The velocities of the new-injected particles are described by the semi-Maxwellian distribution characterized by an anode temperature of $750K$, in agreement with Ref. [33]. Being neutrals without charge, they can accelerate within the channel only due to the walls impacts. Neutrals that collide with the walls of the channel are scattered back in the domain diffusively with a velocity that follows a Maxwellian distribution characterized by a wall temperature of $850K$ [33]. The particles that leave the domain outside of the channel are removed from the simulation.

To reduce the numerical oscillations induced by the method, the number of particles per cell must be optimized. This parameter depends on specific weight (that means the total number of particles simulated) and grid (that means the number of cells). From the sensitivity analysis carried out in Ref. [34] and Ref. [31], a good trade-off between accuracy and computational cost is 30-50 particles per cell. In this work, according to the grid used, has been chosen a specific weight of neutrals of $2.5 \cdot 10^{11}$ to ensure an average number of particles per cell of approximately 30. To ensure that each particle moves a maximum of one cell per time step, a time step of $5 \cdot 10^{-8}$ s has been set, according to [21].

Tab. 3.3 summarizes the main parameters of the test and Fig. 3.2 shows the adopted domain and the centerline. The centerline divides the channel into two halves (radial position = 42.5 mm) and it is a line parallel to the thruster axis. Fig. 3.3 shows the adopted domain in tests with eroded wall geometry.

Parameters	**Values**
Grid	47×22
Integration time [s]	$5 \cdot 10^{-8}$
Specific weight	$2.5 \cdot 10^{11}$
Number of particles simulated	30000
Anode temperature [K]	750
Wall temperature [K]	850

Table 3.3: Main parameters of neutral test.

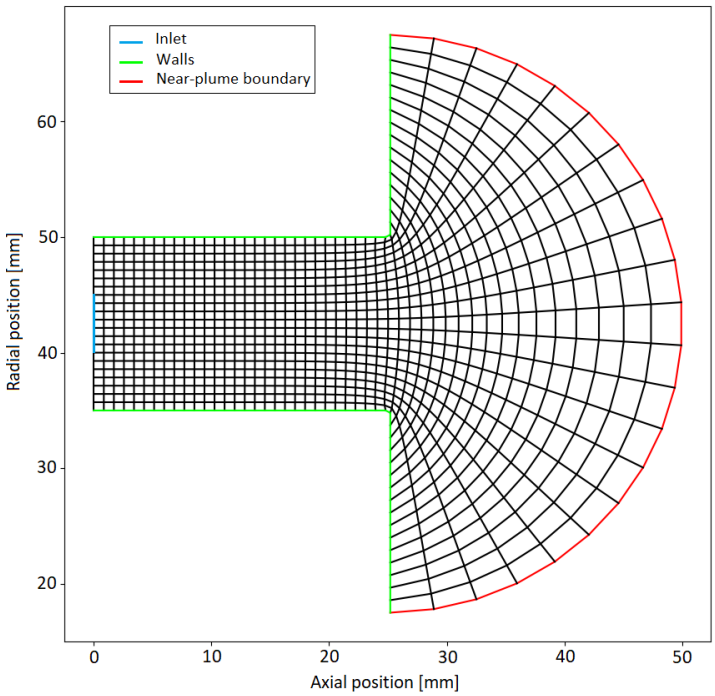

Figure 3.2: Domain adopted in tests with non eroded channel.

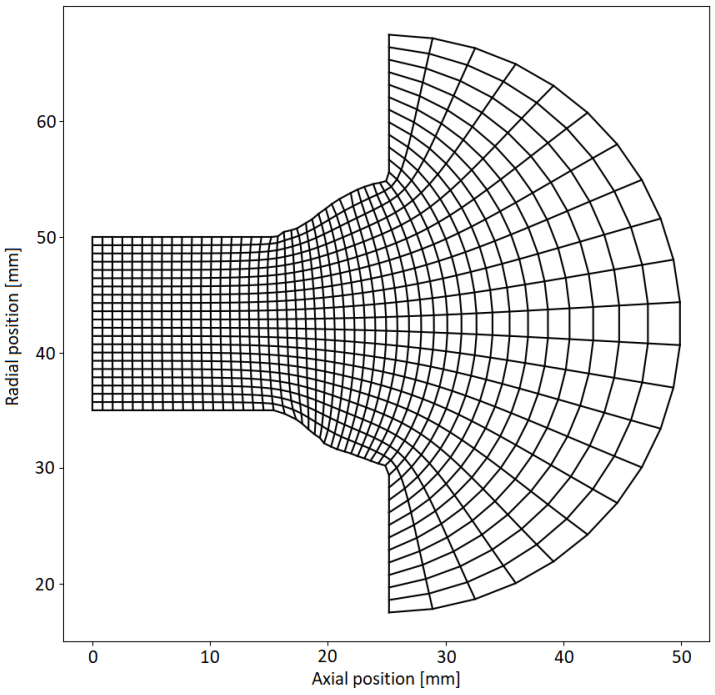

Figure 3.3: Domain adopted in tests with eroded channel.

3.2.1 Non-eroded channel - Neutral test

Since PIC approach has intrinsic numerical oscillations, the end of the simulation is declared when the computed quantities (i.e. density, velocity) fluctuates around a constant value. Particularly, for neutral tests, the number of macro-neutrals is selected for this verification.

Fig. 3.4 shows the temporal evolution of the number of neutrals. It can be seen that after an initial transitional phase (about 20000 time-steps) where the number of neutrals increases, it stabilizes at around 30000 neutrals, which depends on the input value of the specific weight of the neutrals. By subdividing the number of macro-neutrals with the number of cell it is possible to verify that an average number of more than 30 macro particle per cell results.

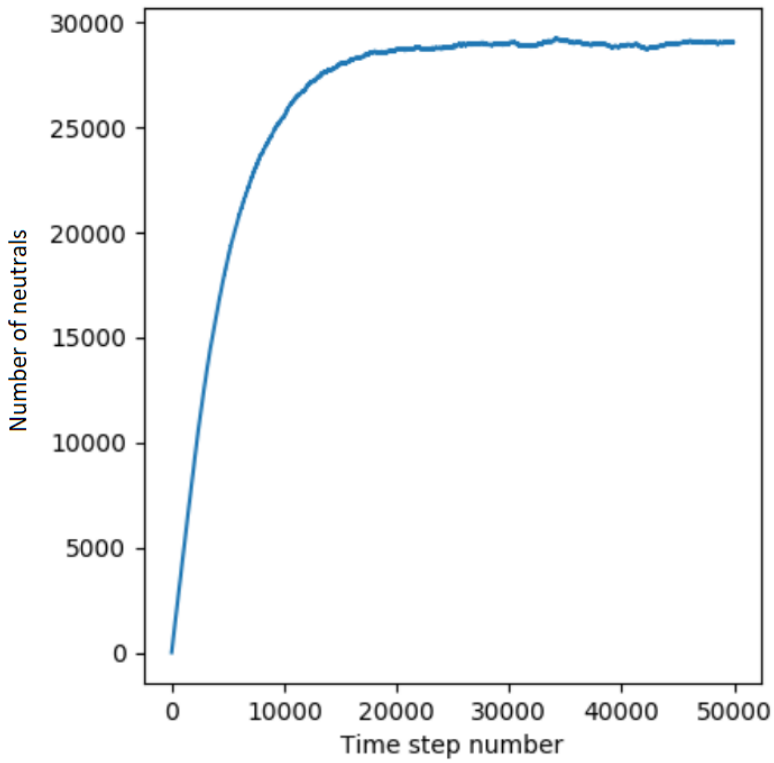

Figure 3.4: Temporal evolution of the number of neutrals during the simulation.

Fig. 3.5 shows the comparison between the average mass flow rate injected at the inlet and the average mass flow rate computed along the channel, in order to verify mass conservation. Neutral mass flow rate is evaluated averaging 299 solutions spaced of 100 time steps. The test has shown that conservation of mass is verified with an error of 6.98%.

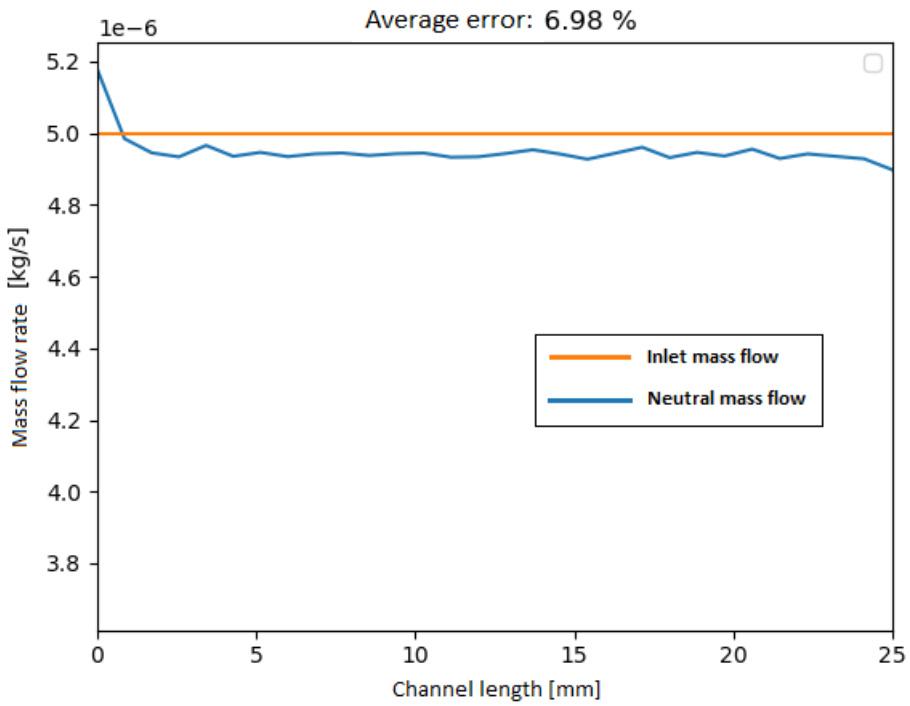

Figure 3.5: Comparison between inlet mass flow rate and neutrals mass flow rate computed along the channel.

Fig. 3.6 and 3.7 show the neutral density within the channel and in the plume, when they are the only species flowing within the domain (Fig. 3.7 is zoomed on the channel). The distributions are obtained respectively by present code and by HPHall2, the code developed by the Jet Propulsion Laboratory (JPL) [21]. Both contour plots are time-average, particularly the results of the present code are obtained averaging 299 solutions spaced of 100 time steps. As expected, the highest neutral density is near the anode, while it decreases along the channel because the only motion is given by the initial velocity and possible collisions with the walls. The results of both tests are comparable: in the zone near the anode the neutral density is about $1.3 \cdot 10^{20}\ m^{-3}$, at the channel outlet is about $2 \cdot 10^{19}\ m^{-3}$ while in the plume zone is reached about $1 \cdot 10^{19}\ m^{-3}$. It is possible to see that on the contour by HPHall2 there are the same values.

Fig. 3.8 and 3.9 show the neutral velocity modules within the channel and in the plume. Again, both contour plots are time-average, particularly the results of the present code are obtained averaging 299 solutions spaced of 100 time steps. The results of present test are comparable with those of HPHall2: near the anode the velocity is about 140 m/s while at the outlet of channel the velocity is about

230 m/s. It is possible to see that on the contour by HPHall2 there are the same values. Furthermore the velocity is not symmetrical because of axisimmetry of HET.

In Fig. 3.10 it is possible to see the time average neutral density (ndn) and modulus of neutral velocity ($vmod$), along the channel centerline, of the two tests compared. Both the density trend and velocity trend of the present code are in good agreement with those of HPHall2. It is worth to notice that the data for HPHall2 in Fig. 3.10 are extrapolated from contour plots, so they are subject to extrapolation errors.

The values sampled at the channel exit are reported in Tab. 3.4: both neutral density and neutral velocity are comparable with the values of HPHall2. These are excellent result showing that the neutral particles and BC have been modeled appropriately.

	HYPICFLU (Present code)	**HPHALL2** [21]
Neutral density [m^{-3}]	$2.5 \cdot 10^{19}$	$2 \cdot 10^{19}$
Neutral velocity [m/s]	230	240

Table 3.4: SPT-100 Neutral Flow Test: neutral density and neutral velocity sampled at the channel exit on centerline.

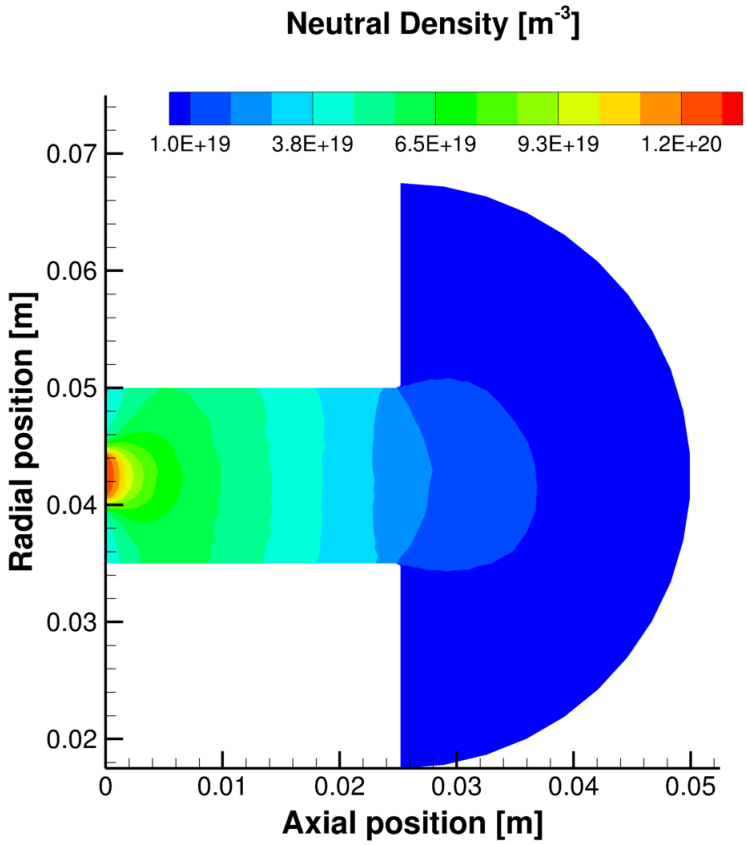

Figure 3.6: SPT-100 Neutral Flow Test: neutral density contour by present code.

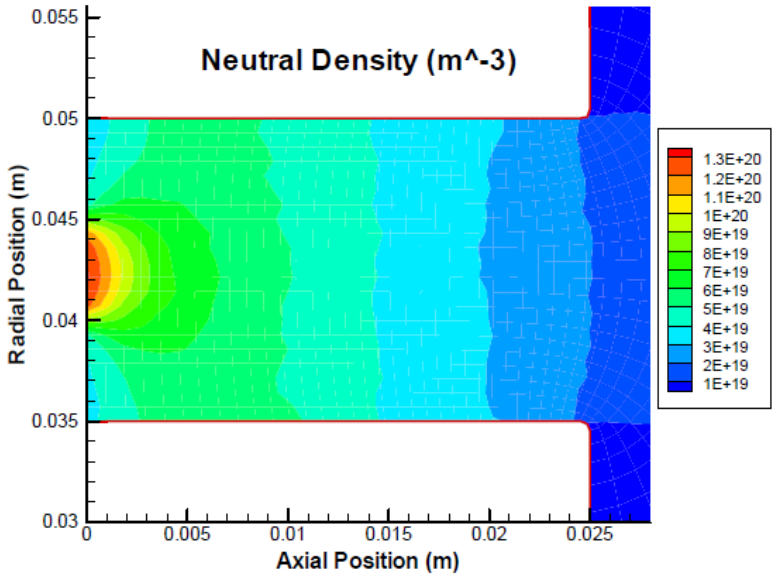

Figure 3.7: SPT-100 Neutral Flow Test: neutral density contour by HPHALL2 [21].

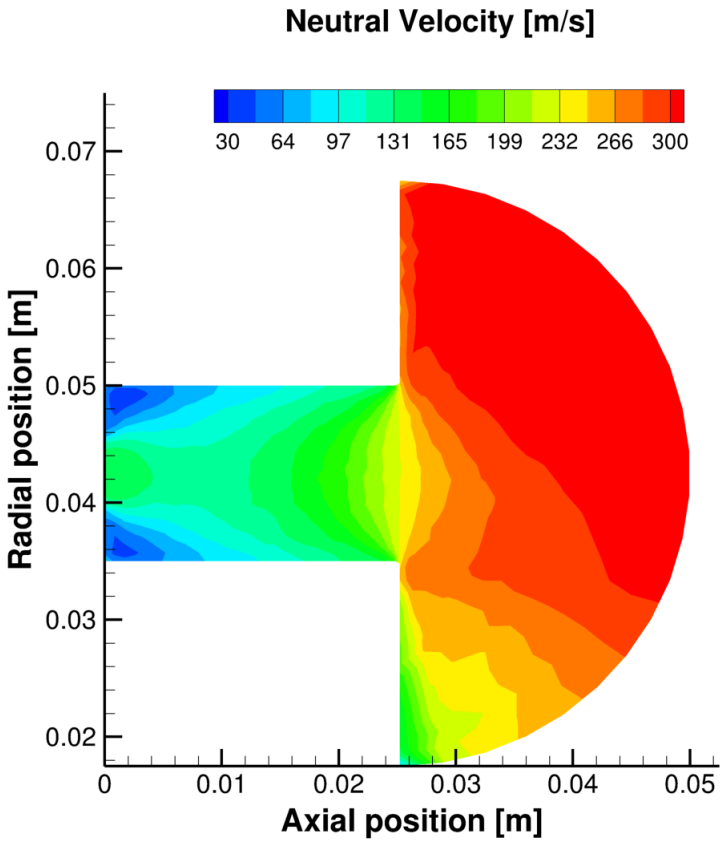

Figure 3.8: SPT-100 Neutral Flow Test: neutral velocity contour by present code.

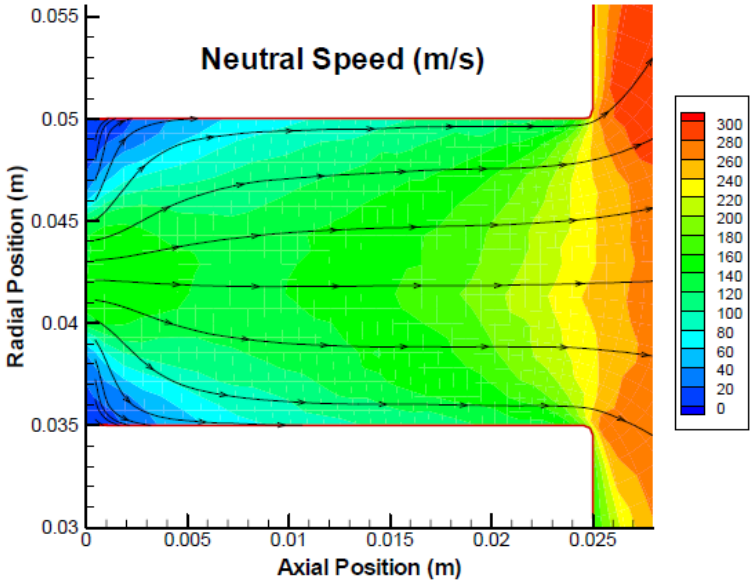

Figure 3.9: SPT-100 Neutral Flow Test: neutral velocity contour by HPHALL2 [21].

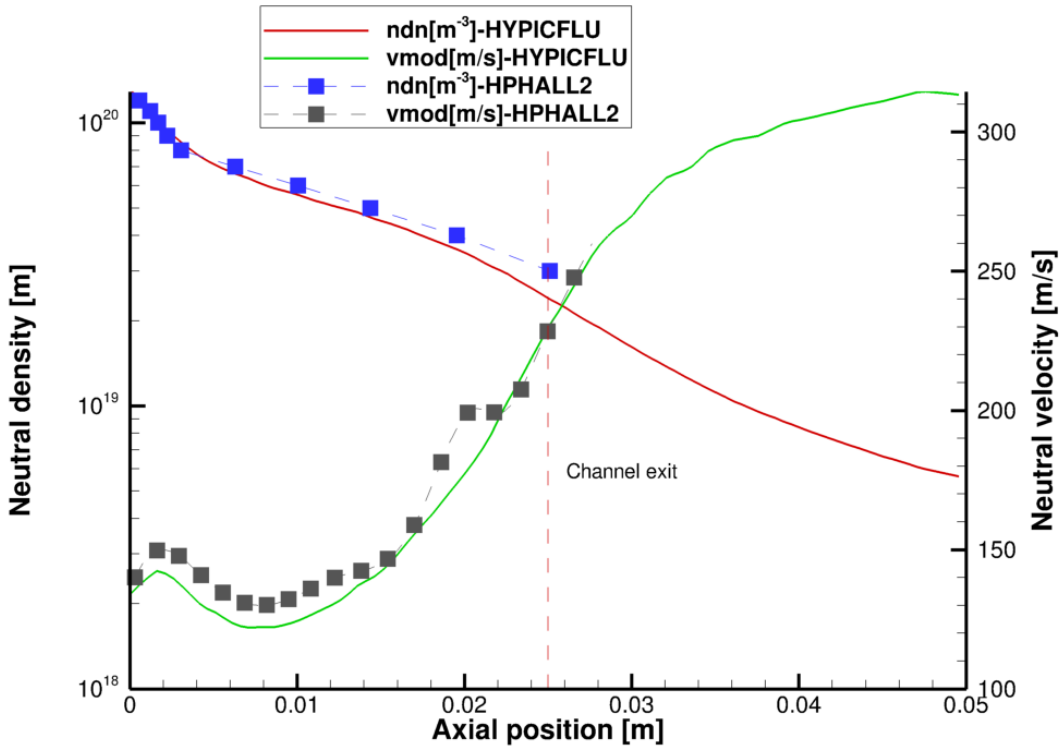

Figure 3.10: SPT-100 Neutral Flow Test: time average neutral density (*ndn*) and modulus of neutral velocity (*vmod*) along the channel centerline; comparison between present code and HPHall2 [21].

3.2.2 Eroded channel - Neutral test

In developing the PIC module, it has been considered the possibility of any domain variation (changing the domain's boundary means modifying the geometry of the device's walls).

This approach will be useful for studying and analyzing the erosion phenomenon in the thruster and therefore for predicting the operative life and the decrease of the performance.

The purpose of this test is to verify that the present code gives optimal results even in the presence of a change of domain. So the inputs and hypothesis of this test are the same as the previous one i.e. non-eroded channel. The only difference is the domain i.e. this test has a larger domain.

The geometry of the eroded channel are taken from Ref. [21]. Figure 3.11 shows the channel erosion computed and measured after 180, 300, 600, 800 and 1000 hours of operation. The geometry after 1000 hours is considered in the present test.

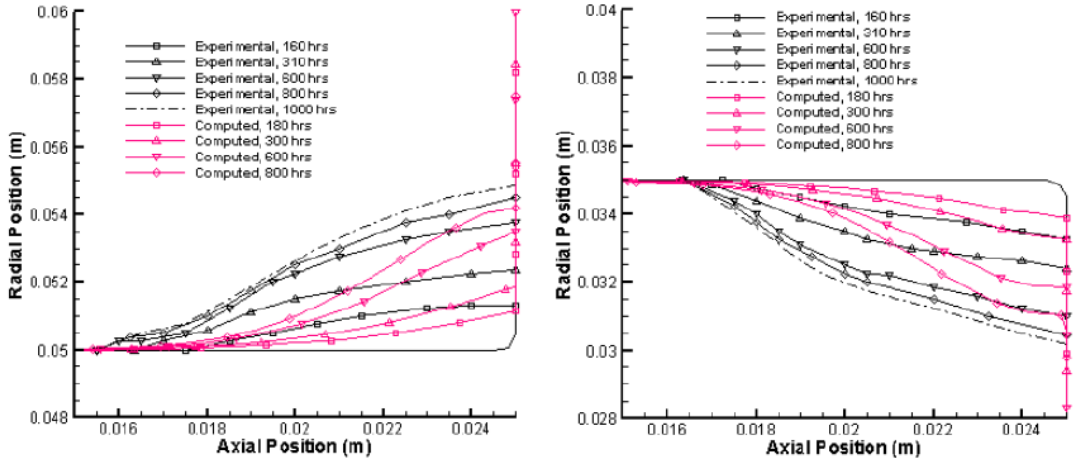

Figure 3.11: Computed and experimental erosion profiles for the outer and inner discharge chamber walls [35].

Fig. 3.12 shows the contour plot of neutral density in the domain, while Fig. 3.13 shows the contour plot of neutral velocity. It can be seen that both variables fit very well into the new domain. Instead, Fig. 3.14 shows time average neutral density (ndn) and modulus of neutral velocity ($vmod$) along the channel centerline. Since the domain is larger than in the non-eroded case, it can be seen that the flow is more expanded. Indeed, at the same axial position, neutral density is lower while neutral velocity is higher.

This test shows that the code works in the presence of domain changes and is ready for future implementation of the erosion phenomenon.

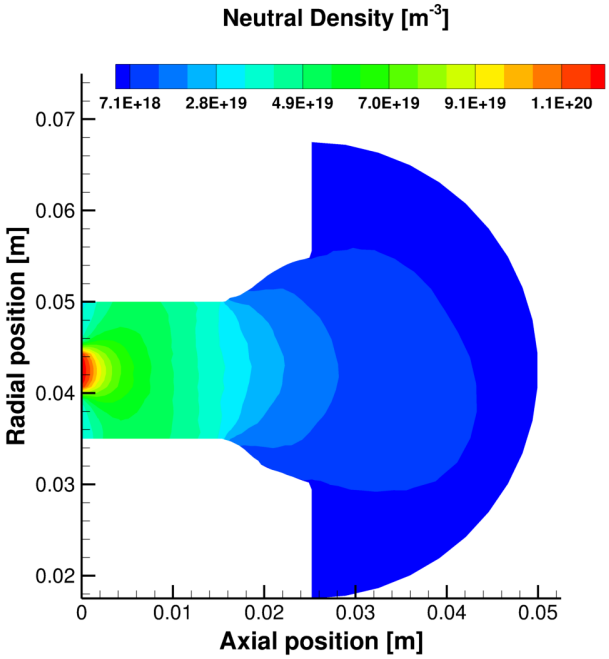

Figure 3.12: SPT-100 Neutral Flow Test (eroded wall geometry): neutral density contour by present code.

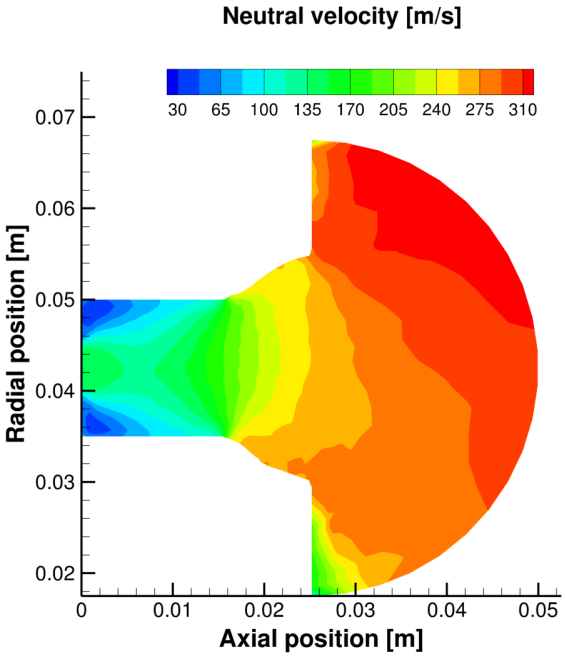

Figure 3.13: SPT-100 Neutral Flow Test (eroded wall geometry): neutral velocity contour by present code.

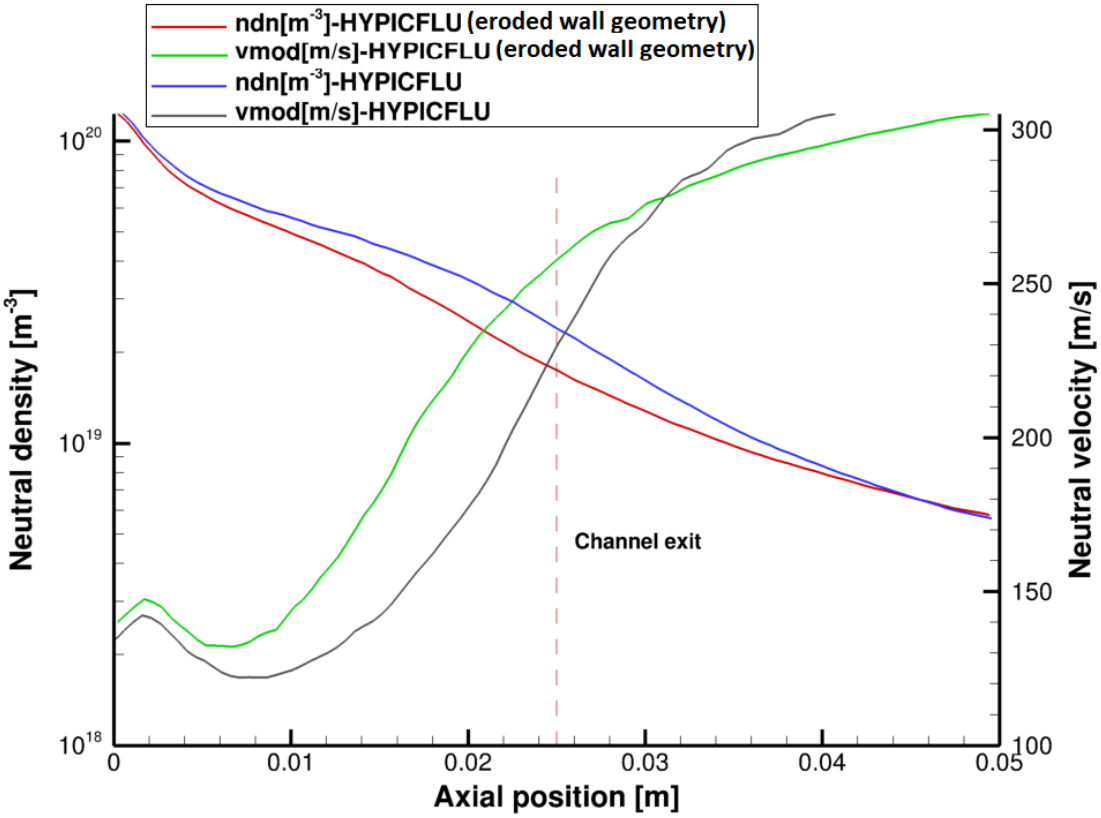

Figure 3.14: SPT-100 Neutral Flow Test (eroded wall geometry): time average neutral density and neutral velocity along the channel centerline; comparison between eroded channel test and non-eroded channel test.

3.3 Ion-Neutral Flux

The ion-neutral flow test case has been designed to verify the correct modeling, by PIC module, of the motion of ions and neutrals within the accelerating channel of a HET. Time-invariant electron temperature (T_e) and axial electric fields (E_z) get from Ref. [33] (Fig. 3.15), are set.

Macro-neutrals are injected from the inlet and part of them ionize due to non-null electron temperature. Ions created are accelerated toward the exit by the axial component of the electric field.

Condition of quasi-neutrality ($n_i \simeq n_e$) is imposed. The domain is the same adopted in neutrals test (Fig. 3.2).

The temperature of the channel walls is assumed to be 850 K according to Ref. [33]. It is also assumed that every ion that collides with a wall is absorbed by this

last one, so ions recombine into a neutral with a velocity that, again, is sampled from a semi-Maxwellian distribution at the wall temperature. The law of surface recombination is linked to the different specific weights of ions and neutrals, which for this test are respectively $2.5 \cdot 10^9$ e $2.5 \cdot 10^{11}$. The particles that leave the domain outside of the channel are removed from the simulation.

The main parameter of the test are reported in Tab. 3.5

Parameters	**Values**
Grid	47×22
Integration time [s]	$5 \cdot 10^{-8}$
Neutral specific weight	$2.5 \cdot 10^{11}$
Ion specific weight	$2.5 \cdot 10^{9}$
Number of particles simulated	≈ 45000
Anode temperature [K]	750
Wall temperature [K]	850

Table 3.5: Main parameters of ion-neutral test.

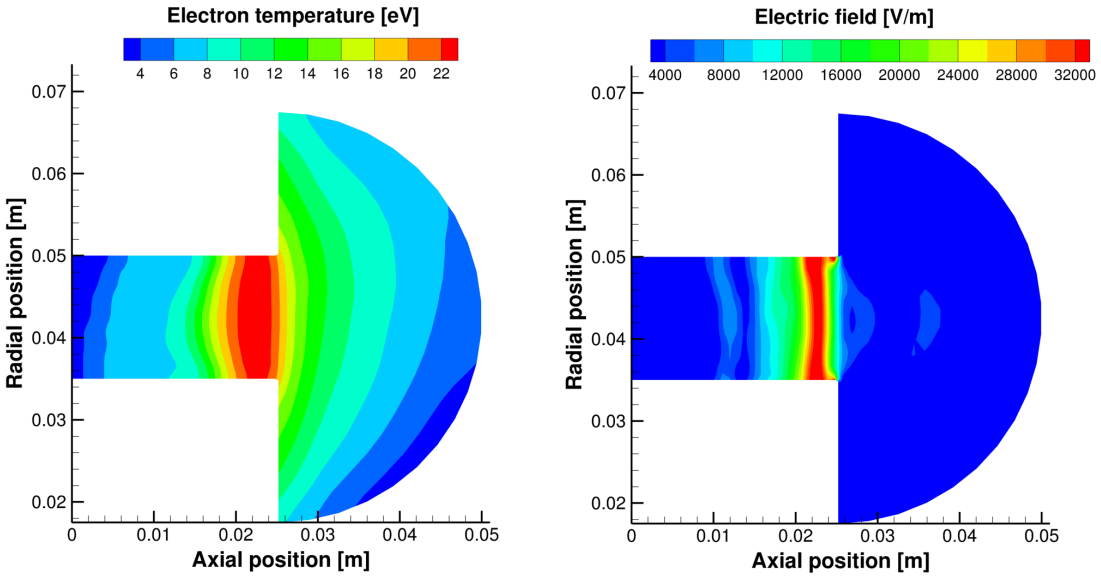

Figure 3.15: Contour plot of electron temperature and axial electric field set in the ion-neutral test.

3.3.1 Non-eroded channel - Ion-Neutral test

In this test the number of macro-neutrals, , as also stated in the Par. 3.2.1, and the number of macro-ions are used as parameters to check the end of the simulation.

Fig. 3.16 shows the temporal evolution of the number of neutrals during simulation. There is no initial transition phase in which the number of ions and neutrals starts from 0 and increases because a list of ions and neutrals has been set as an initial guess. It can be seen that the oscillations of neutrals number are slight, while those of the ions are more pronounced. These strong oscillations can be attributed to the effect of the input electric field which is not updated in the simulation (i.e. by means of the fluid module). Moreover, in the present test, the radial component of the electric field has not been set.

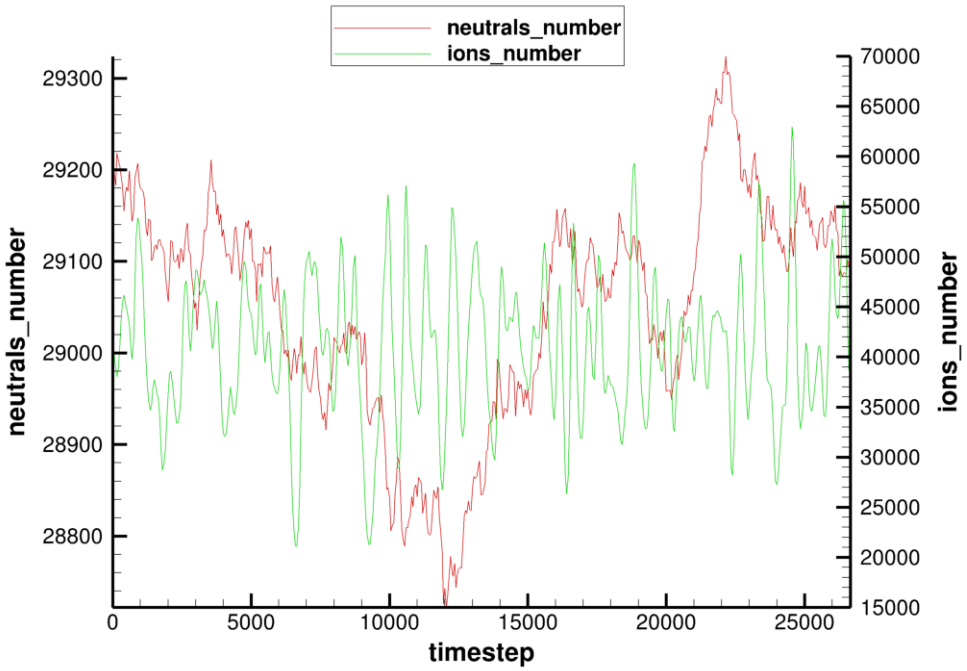

Figure 3.16: Temporal evolution of the number of macro neutrals and macro ions during the simulation.

Fig. 3.17 shows the comparison between the average mass flow rate injected at the inlet, the average neutral mass flow rate, and the average ion mass flow rate along the channel, to verify mass conservation. It is a very important check to be done because the functions that create ions and eliminate neutrals due to ionization is different. As expected, toward the exit channel the ion mass flow increases while the neutral mass flow decreases. Within the channel, at any section, the sum of the two mass flows must be as close as possible to the inlet mass flow. The values

are computed averaging 534 solutions spaced of 50 time steps and averaging along the radial direction. The ion-neutral test has shown that conservation of mass is verified with an error of 1.32% which is an excellent result.

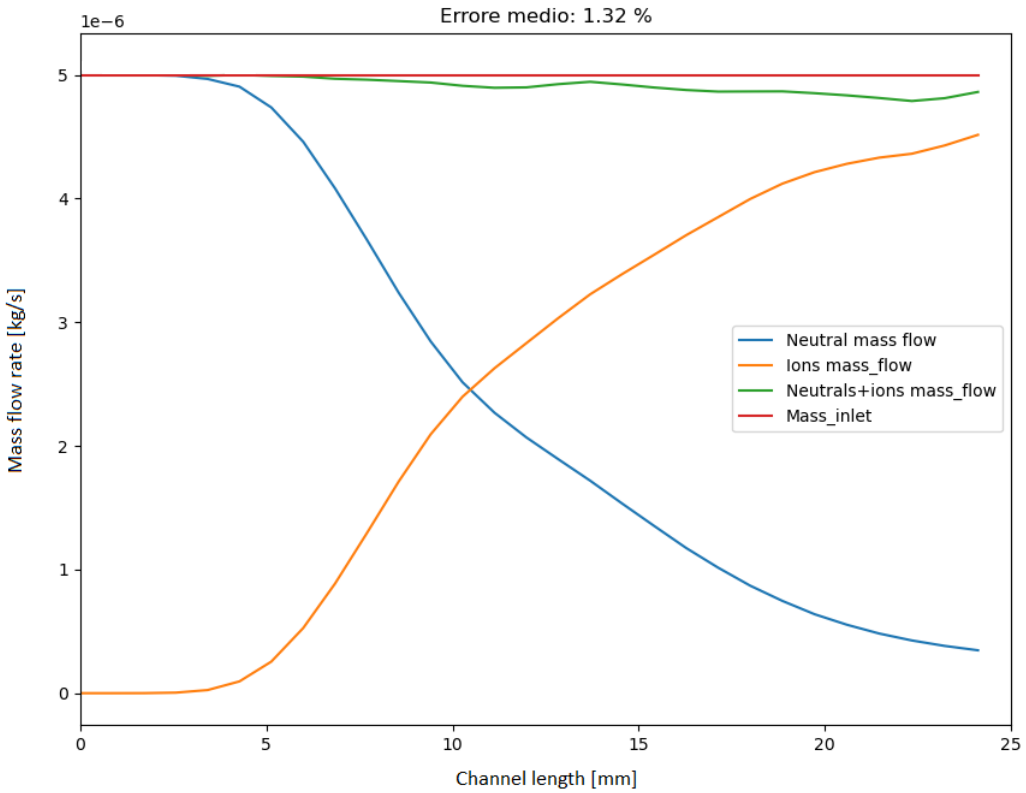

Figure 3.17: Comparison between inlet mass flow rate, neutrals mass flow rate, and ion mass flow rate computed along the channel.

Fig. 3.18 and 3.19 show the neutral density within the channel and in the plume when they are not the only species flowing within the domain. The distributions are obtained respectively by present code and by HPHall2, the code developed by the Jet Propulsion Laboratory (JPL) [33]. Either contour plots are time-average, particularly the results of the present code are obtained averaging 534 solutions spaced of 50 time steps. As expected, the highest neutral density is near the anode, while, along the channel, it decreases quickly to the coordinate $z = 0.015\ m$, the section in which the ionization zone is located. The results of both codes are comparable: in the zone near the anode, the neutral density is about $1 \cdot 10^{20}\ m^{-3}$, near the ionization zone and in the plume is about $1 \cdot 10^{19}\ m^{-3}$. It is possible to see that on the contour by HPHall2 there are the same values. It can be seen that the only difference is the section in which the neutral density reaches the minimum

value. This effect is due to the different position of the ionization zone.

Fig. 3.20 and 3.21 show the ion density within the channel and in the plume. As expected, the highest value of ion density is in the ionization zone while moving away from this zone, the ion density gradually decreases. The maximum and minimum values prediceted by the present code and by HPHall2 have the same order of magnitude but differ slightly. This difference is due to different position of the ionization zone that, in the present test, is shifted back from the position predicted by HPHall2; in this section the neutral density is higher, consequently the ionization (ionization rate) is stronger and so also the ion density is higher.

Fig. 3.22 and 3.23 show the ionization rate within the channel and in the plume. As expected, due to the axial electric field set, the maximum value of ionization rate is at the coordinate $z = 0.01\ m$ and, moving away from this section, gradually decreases. The overall order of magnitude is the same computed by HPHall2 (i.e. $\sim 10^{23} \div 10^{24} m^{-3} s^{-1}$). The difference between the prediction made by the two codes is the position of the ionization rate peak that for HPHall2 is located at $z = 0.015\ m$. This effect is due to the different axial electric fields used and the lack of radial electric field.

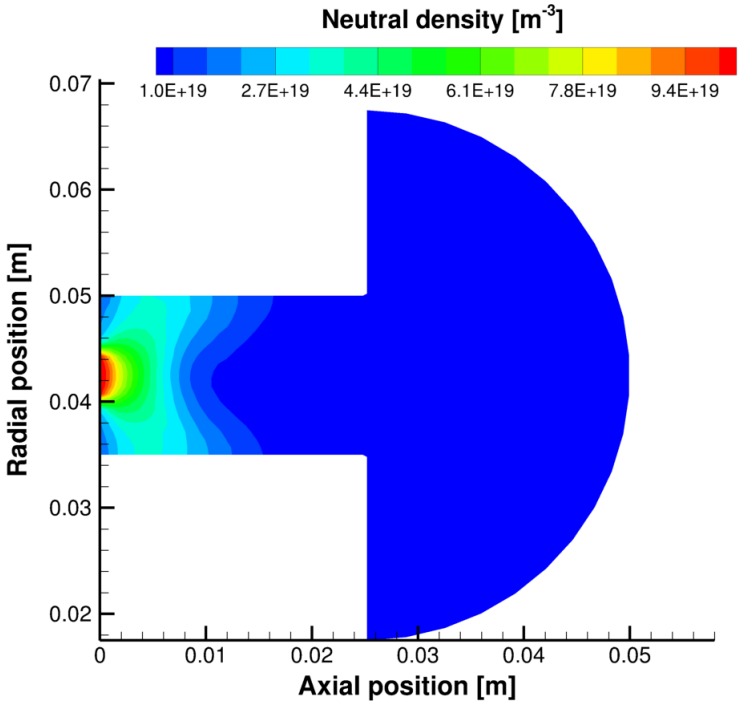

Figure 3.18: SPT-100 Ion-Neutral Flow Test: neutral density contour by present code.

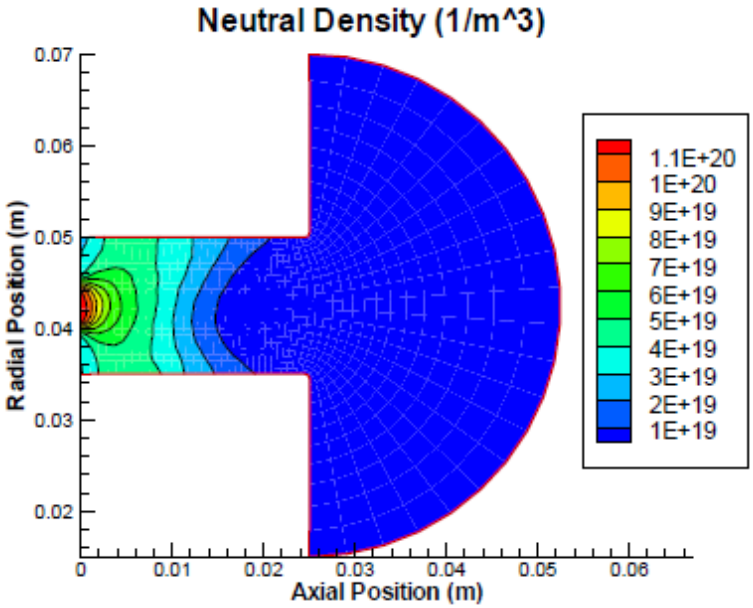

Figure 3.19: SPT-100 Ion-Neutral Flow Test: neutral density contour by HPHALL2 [33].

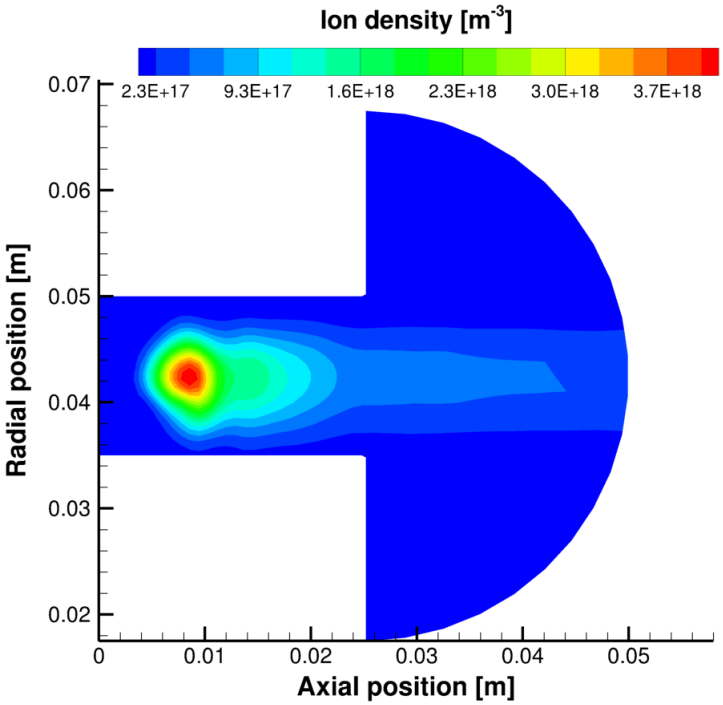

Figure 3.20: SPT-100 Ion-Neutral Flow Test: ion density contour by present code.

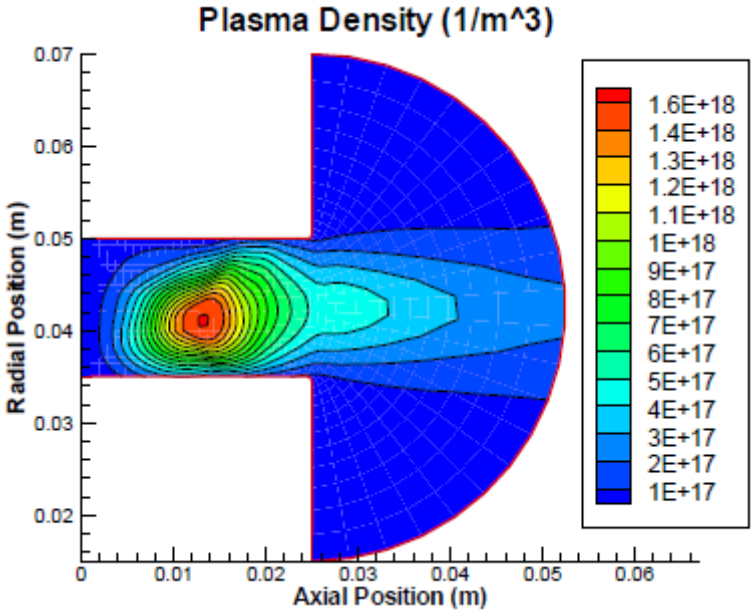

Figure 3.21: SPT-100 Ion-Neutral Flow Test: ion density contour by HPHALL2 [33].

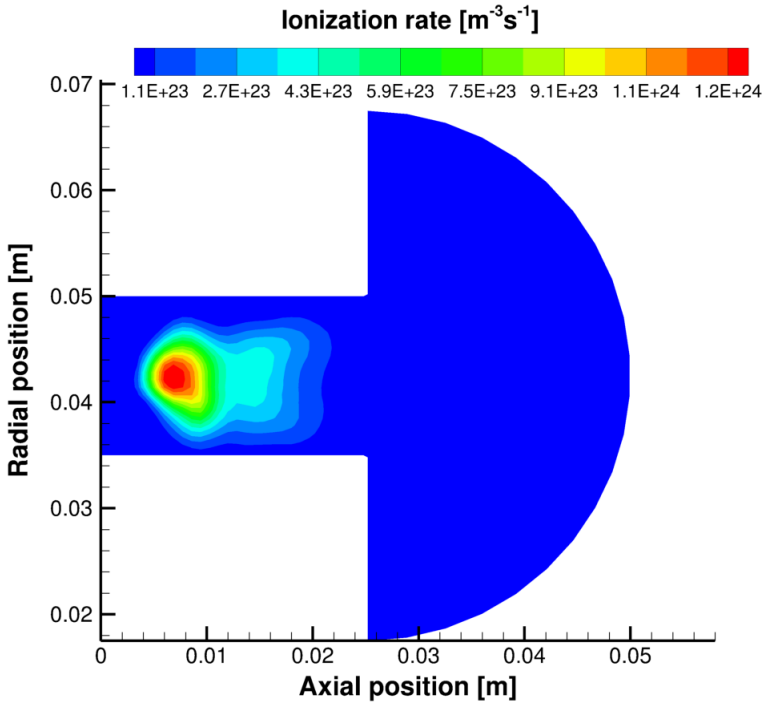

Figure 3.22: SPT-100 Ion-Neutral Flow Test: ionization rate contour by present code.

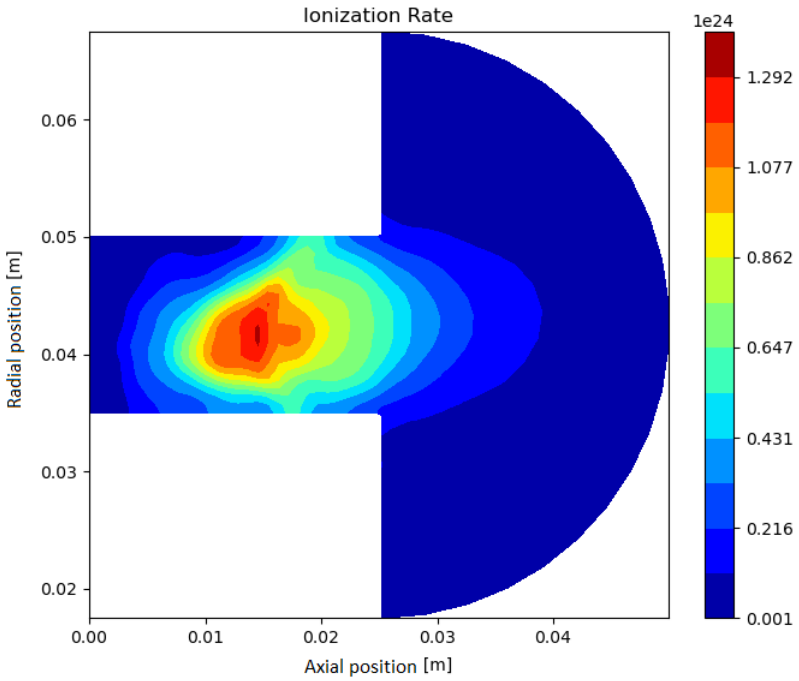

Figure 3.23: SPT-100 Ion-Neutral Flow Test: ionization rate contour by HPHALL2.

Fig. 3.24 shows the time average neutral density (ndn) and ion density (ndi), along the channel centerline, of two tests compared. Both orders of magnitude and qualitative trend of both variables are very close to those of the reference (HPHall2). The difference in the neutral density is due to the surface recombination function implemented: this function, in the present code, absorbs fewer ions than that of the HPHall2 code, so there is a release of fewer neutral. As demonstrated in Ref. [20] indeed, this different neutral density does not depend on the number of particles simulated. The lower neutral density also causes another effect: the ionization rate is defined by the Eq. 2.3, so since in the section where is located the peak of ion density there is the same ionization rate value and less neutral density between two codes (the present code and HPHall2 code), is expected higher ion density to respect the ionization rate equation.

Fig. 3.25 shows the time average ionization rate (ki), along the channel centerline, of two tests compared. It should be noted that the ionization rate values of HPHall2 have been extrapolated from the contour plot and so there are errors related to data reconstruction. Anyway, both orders of magnitude and the qualitative trend of both variables are very close to those of the reference (HPHall2). It can be seen that, as shown in Figs. 3.22 and 3.23, the ionization rate peak of the present code is shifted back compared with that of the HPHall2 code. These differences are due to the axial electric field set and the lack of radial electric field.

Fig. 3.26 shows the time average neutral velocity (vzn) and ion velocity (vzi), along the channel centerline. It should be noted that both neutral and ion velocity trends have some depression, due to numerical oscillations and axial electric field set. Anyway, it can be seen that the values of neutral velocity, of present code and HPHall2 code, at the channel exit, are very similar. In the case of ion velocity, instead, the order of magnitude and the trend of the results obtained with the present code are in good agreement with the experimental data of Ref. [22]. These experimental data were obtained with two tests in a fixed pressure chamber ($1.7 \cdot 10^{-5}$ $torr$ and $5 \cdot 10^{-5}$ $torr$), while in the present code the pressure is not set as a boundary condition but it is an a posteriori obtainable value. Moreover, it can be noted that the experimental data reach negative values of axial velocity. This difference is due to the fact that the axial electric field set is everywhere positive because, if we had set an electric field with even negative values, the code would have had converge to non physical solutions.

Tab. 3.6 groups the data discussed above, sampled at the channel exit, compared with those of HPHall2. Moreover, the table shows mass utilization efficiency defined as the ratio of the mass flow rate of ions to the anode mass flow rate [14]. Also, this last parameter is in good agreement with those of HPHall2.

	HYPICFLU (Present code)	**DATA REFERENCE** [21, 33, 22]
Neutral density [m^{-3}]	$6.2 \cdot 10^{17}$	$1.2 \cdot 10^{18}$
Neutral velocity [m/s]	311	299
Ion density [m^{-3}]	$5.9 \cdot 10^{17}$	$7.6 \cdot 10^{17}$
Ion velocity [m/s]	15859	16869^{*} 15711^{**}
Mass utilization efficiency	91.7%	90.1%

Table 3.6: SPT-100 Ion-Neutral Flow Test: neutral density, neutral velocity, ion density, ion velocity, and mass utilization efficiency sampled at the channel exit on centerline (Exp. background pressure: $^{*}5 \cdot 10^{-5}$ *torr*, $^{**}1.7 \cdot 10^{-5}$ *torr*).

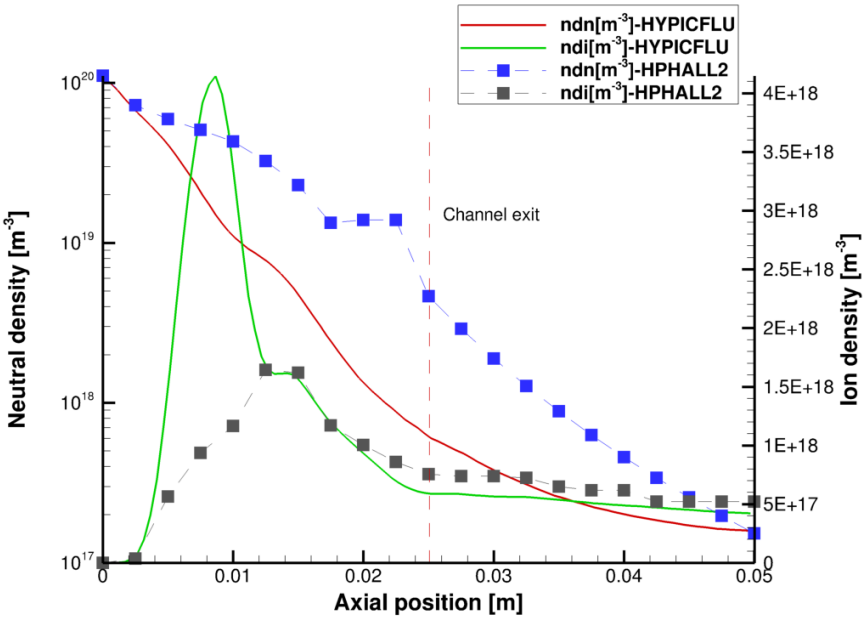

Figure 3.24: SPT-100 Ion-Neutral Flow Test: time average neutral density (*ndn*) and ion density (*ndi*) along the channel centerline; comparison between present code and HPHall2.

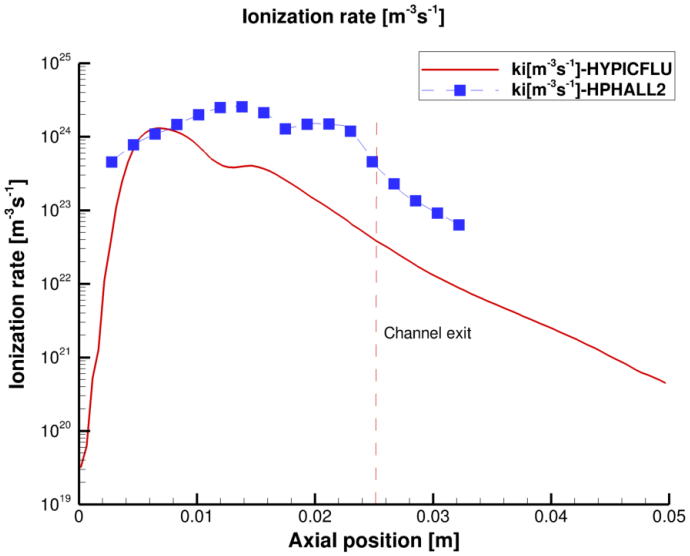

Figure 3.25: SPT-100 Ion-Neutral Flow Test: time average ionization rate (ki) along the channel centerline; comparison between present code and HPHall2.

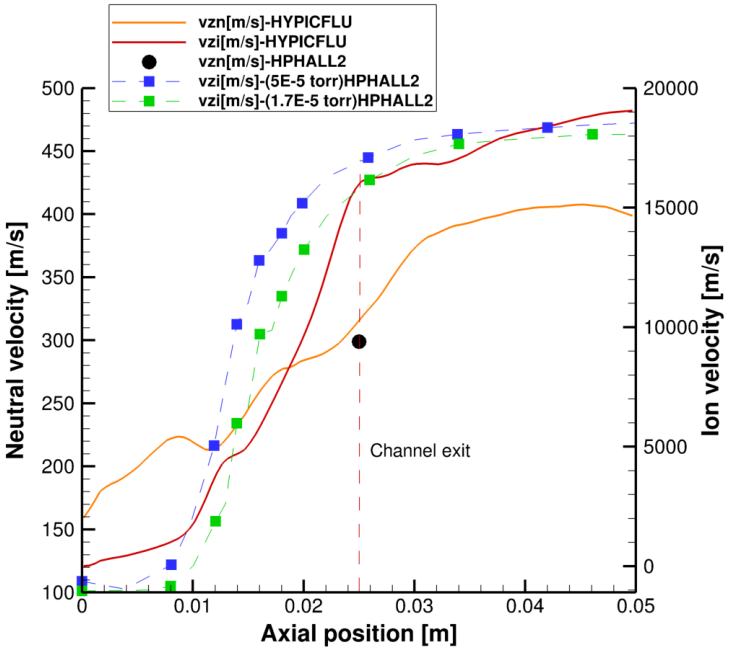

Figure 3.26: SPT-100 Ion-Neutral Flow Test: time average neutral velocity (vzn) and ion velocity (vzi) along the channel centerline; comparison between present code and experimental data [22].

3.3.2 Eroded channel - Ion-Neutral test

In this test case, simple comparison between the eroded case and the non-eroded case but also a qualitative comparison with the test carried out by Anton *et. al* [23] using HPHall2 code have been made. Particularly the second one focuses on the ion current density, which is defined by the equation:

$$J_i = n_i q v_i \tag{3.1}$$

where n_i is the ion density, q is the electric charge and v_i is ion velocity.

Fig. 3.28 shows the comparison between the test with eroded channel test and non-eroded channel test of present code. Although switching from one case to another it is observed that the ion density (ndi) decreases while ion velocity (vzi) increases (Fig. 3.27), the overall effect is that the ion current density (J_i) decreases in good agreement with Fig. 3.29. The only difference between the present code and the HPHall2 code is that the first has an ion current density greater than those of the second. This effect is due to different value of ion density, explained by the lack of radial electric field and different axial electric field set.

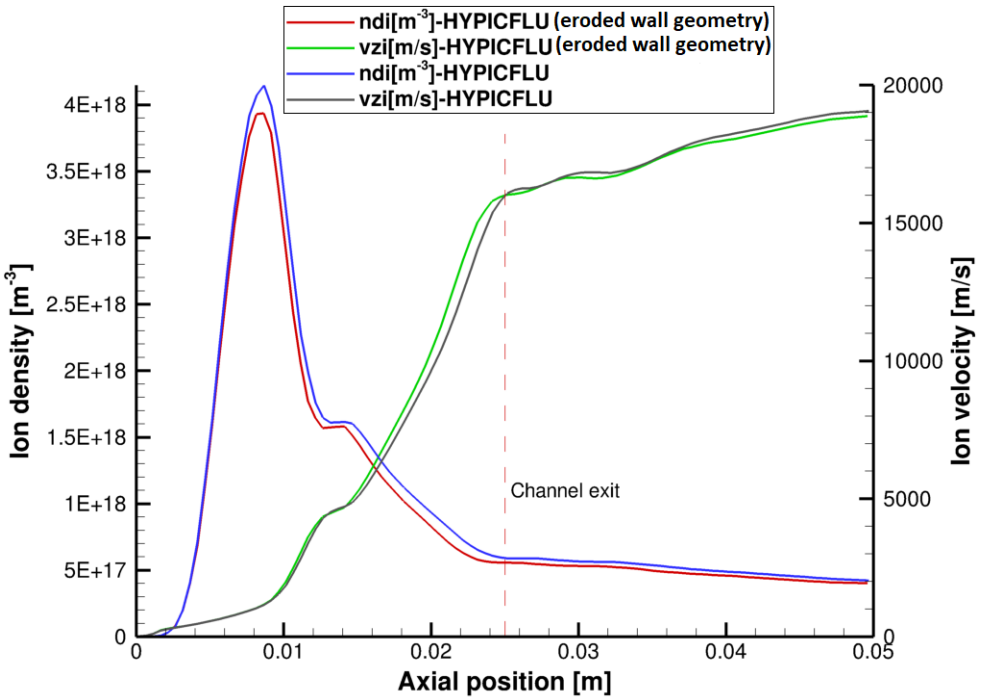

Figure 3.27: SPT-100 Ion-Neutral Flow Test (eroded wall geometry): time average ion density (ndi) and ion velocity (vzi) along the channel centerline; comparison between eroded channel test and non-eroded channel test.

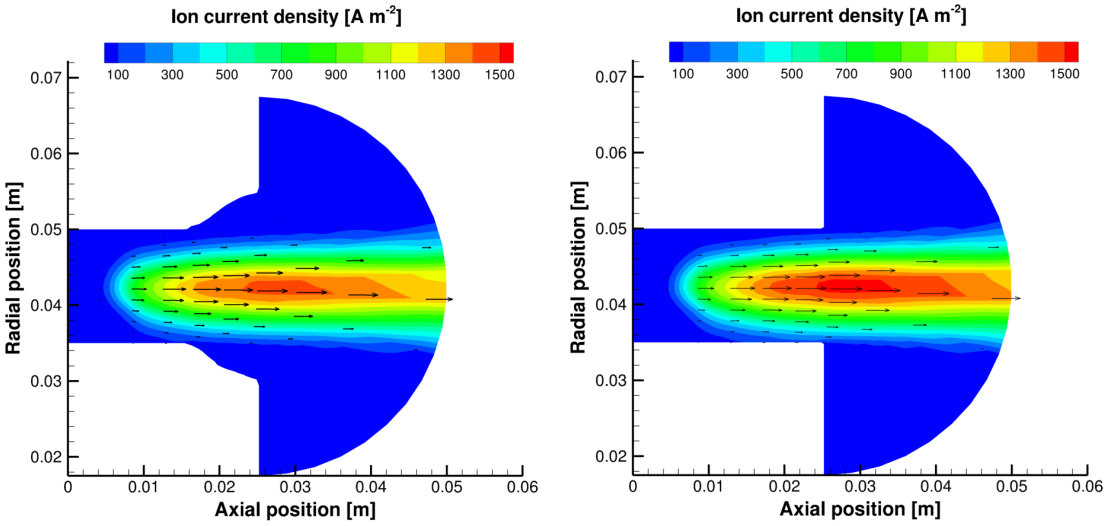

Figure 3.28: SPT-100 Ion-Neutral Flow Test: ion current density contour with eroded channel (left) and non-eroded channel (right) by present code.

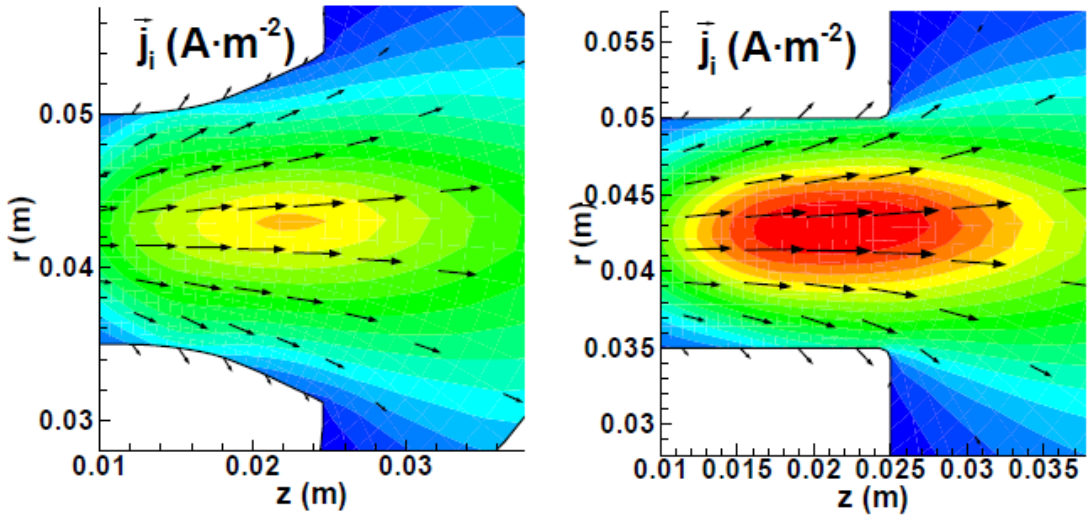

Figure 3.29: SPT-100 Ion-Neutral Flow Test: ion current density (J_i) contour with eroded channel (left) and non-eroded channel (right) by HPHall2 [23].

3.4 Computing Cost

Here are reported some brief considerations on computing cost. A high computational cost was found and the calculation of logical coordinate and the particles advancer functions are the most time-consuming. Since the main goal of this work

thesis was to test the model, no care was taken in reducing computational time of the code. The operations are sequentially executed on Intel(R) Xeon(R) CPU E5-2640 v4 @ 2.40 GHz. Tab. 3.7 shows for each test the number of time step per hour, the total number of time steps and total computational time.

	Neutral test	**Ion-Neutral test**
Total num. of macro-particles	29031	67217
Final time step	49900	26650
Time-to-final time step (days)	5	8
Time step/hour	≈ 350	≈ 150

Table 3.7: SPT-100 discharge simulation: computational time.

Chapter 4

Conclusion and Future Steps

This work thesis has described the development of PIC module of CIRA hybrid code (HYPICFLU) aiming to simulate the plasma discharge in HETs' acceleration channel and near-plume region. SPT-100 has been chosen as reference thruster because of the amount of data available; particularly HPHall2 code has been chosen for code-code comparisons.

Two cases have been analysed: neutral flow (plasma off) and ion-neutral flow (plasma on). The results obtained in the first case are very close to those obtained by HPHall2; this means that the function dealing with neutral particles have been modelled appropriately. The results obtained in the second case are in good agreement with literature showing. The only differences are attributable to the set boundary conditions (e.g axial and radial electric field, neglected phenomena) and a different implementation of surface recombination function. Anyway, in both simulations, a good description of plasma behaviour has been obtained.

Moreover, two simulations were carried out to test the code under conditions of domain variations in order to simulate the effect of erosion phenomenon on the channel geometry. Both simulations gave good results and were able to describe the physics of the problem appropriately.

It was found that the duration of simulation is very high (high computational cost). This slowness is attributable to the structure of the code and data, and probably also to the programming language used, i.e. *Python*.

4.1 Future Developments

Future developments of the PIC module developed in the work thesis mainly concern the following two points:

- an optimization of code in term of time to increase the convergence speed (parallelization of code, change of data structure). The possibility of switching to more performing programming languages should also be considered.
- the use of different PIC grid built from magnetic field; this would allow to avoid interpolation errors that inevitably occurs when the variables are transferred from PIC to Fluid nodes, and vice-versa.

Publication

This work thesis has been chosen to participate in the IEPC Student Competition, in which it will present [36]. The title of the presentation of this work is *"Particle-In-Cell Simulation of Heavy Species in Hall Effect Thruster Plasma"* and the co-authors are Dr. Ing. Mario Panelli and Dr. Ing. Francesco Battista. The presentation will take place the July 16th.

Moreover, an abstract of this work thesis has been accepted by the Italian Association of Aeronautics and Astronautics (AIDAA) committee so a long paper will present at the XXVI International Congress 2021 of AIDAA [37] whose title is *"Particle-In-Cell Simulation of Heavy Species in Hall Thruster Discharge"* and co-authors are Dr. Ing. Mario Panelli and Dr. Ing. Francesco Battista. The conference will take place the August 31st - September 3rd.

Bibliography

[1] Dan M Goebel and Ira Katz. *Fundamentals of electric propulsion: ion and Hall thrusters*. Vol. 1. John Wiley & Sons, 2008 (cit. on pp. 1, 2, 8, 10, 15).

[2] Dan Lev, Roger M. Myers, Kristina M. Lemmer, Jonathan Kolbeck, Hiroyuki Koizumi, and Kurt Polzin. «The technological and commercial expansion of electric propulsion». In: *Acta Astronautica* 159 (2019), pp. 213–227 (cit. on pp. 1, 2).

[3] M Dudeck, F Doveil, N Arcis, and S Zurbach. «Plasma propulsion for geostationary satellites for telecommunication and interplanetary missions». In: *IOP Conference Series: Materials Science and Engineering*. Vol. 29. 1. IOP Publishing. 2012, p. 012010 (cit. on p. 1).

[4] Robert G Jhan. *Physics of electric propulsion*. Vol. 1. McGraw-Hill, 1968 (cit. on pp. 3–5).

[5] Francis F Chen. *Introduction to plasma physics and controlled fusion*. Third edition. Springer, 2016 (cit. on p. 6).

[6] A Von Keudell and V Schulz-Von Der Gathen. «Foundations of low-temperature plasma physics—an introduction». In: *Plasma Sources Science and Technology* 26.11 (2017), p. 113001 (cit. on p. 6).

[7] Manuel Martinez-Sanchez and James E Pollard. «Spacecraft electric propulsion-an overview». In: *Journal of propulsion and power* 14.5 (1998), pp. 688–699 (cit. on p. 6).

[8] William A Hargus Jr and Michael R Nakles. *Hall Effect Thruster Ground Testing Challenges*. Tech. rep. AIR FORCE RESEARCH LAB EDWARDS AFB CA PROPULSION DIRECTORATE, 2009 (cit. on p. 8).

[9] Lorenzo Casalino. «Propulsione Spaziale». In: 2014 (cit. on p. 9).

[10] Chen Francis F. *Introduction to plasma physics and controlled fusion*. 2016 (cit. on p. 10).

[11] Tommaso Misuri, Francesco Battista, Christian Barbieri, Enrico Alessio De Marco, and Mariano Andrenucci. «High power Hall thruster design options». In: *Proceedings of the 30th International Electric Propulsion Conference (Florence), IEPC*. 2007, pp. 07–311 (cit. on p. 10).

[12] Jean-Pierre Boeuf. «Tutorial: Physics and modeling of Hall thrusters». In: *Journal of Applied Physics* 121.1 (2017), p. 011101 (cit. on pp. 10, 12, 28).

[13] Nathan P Brown and Mitchell LR Walker. «Review of plasma-induced hall thruster erosion». In: *Applied Sciences* 10.11 (2020), p. 3775 (cit. on p. 10).

[14] Richard Robert Hofer. «Development and characterization of high-efficiency, high-specific impulse xenon Hall thrusters». PhD thesis. University of Michigan Michigan, USA, 2004 (cit. on pp. 11, 47).

[15] EY Choueiri. «Plasma oscillations in Hall thrusters». In: *Physics of Plasmas* 8.4 (2001), pp. 1411–1426 (cit. on p. 11).

[16] JP Boeuf and L Garrigues. «Low frequency oscillations in a stationary plasma thruster». In: *Journal of Applied Physics* 84.7 (1998), pp. 3541–3554 (cit. on p. 11).

[17] E Ahedo, P Martınez-Cerezo, and M Martınez-Sánchez. «One-dimensional model of the plasma flow in a Hall thruster». In: *Physics of Plasmas* 8.6 (2001), pp. 3058–3068 (cit. on p. 11).

[18] F Taccogna, S Longo, M Capitelli, and R Schneider. «Particle-in-Cell Simulation of Stationary Plasma Thruster». In: *Contributions to Plasma Physics* 47.8-9 (2007), pp. 635–656 (cit. on p. 11).

[19] John Michael Fife. «Hybrid-PIC modeling and electrostatic probe survey of Hall thrusters». PhD thesis. Massachusetts Institute of Technology, 1998 (cit. on pp. 12, 15–17, 21, 24).

[20] Mario Panelli, Davide Morfei, Beniamino Milo, Francesco Antonio D'Aniello, and Francesco Battista. «Axisymmetric Hybrid Plasma Model for Hall Effect Thrusters». In: *Particles* 4.2 (2021), pp. 296–324. ISSN: 2571-712X. DOI: 10.3390/particles4020026. URL: https://www.mdpi.com/2571-712X/4/2/26 (cit. on pp. 12, 14, 19, 47).

[21] Richard Hofer, Ira Katz, Ioannis Mikellides, and Manuel Gamero-Castaño. «Heavy particle velocity and electron mobility modeling in hybrid-PIC Hall thruster simulations». In: *42nd AIAA/ASME/SAE/ASEE Joint Propulsion Conference & Exhibit*. 2006, p. 4658 (cit. on pp. 12, 25, 28, 29, 32–36, 48).

[22] Natalia MacDonald-Tenenbaum, Quinn Pratt, Michael Nakles, Nickolas Pilgram, Michael Holmes, and William Hargus Jr. «Background pressure effects on ion velocity distributions in an SPT-100 Hall thruster». In: *Journal of Propulsion and Power* 35.2 (2019), pp. 403–412 (cit. on pp. 12, 47–49).

[23] Alfredo Anton and Eduardo Ahedo. «Contour algorithms for a Hall thruster hybrid code». In: *42nd AIAA/ASME/SAE/ASEE Joint Propulsion Conference & Exhibit*. 2006, p. 4834 (cit. on pp. 12, 50, 51).

[24] Rei Kawashima, Kimiya Komurasaki, Tony Schönherr, and Hiroyuki Koizumi. «Hybrid Modeling of a Hall Thruster Using Hyperbolic System of Electron Conservation Laws». In: (July 2015) (cit. on p. 17).

[25] Samuel J Araki and Richard E Wirz. «Cell-centered particle weighting algorithm for PIC simulations in a non-uniform 2D axisymmetric mesh». In: *Journal of Computational Physics* 272 (2014), pp. 218–226 (cit. on p. 21).

[26] «Interpolation using an arbitrary quadrilateral». In: (). URL: `https://www.particleincell.com/2012/quad-interpolation/#ref2` (cit. on p. 22).

[27] Alejandro Allievi and Rodolfo Bermejo. «A generalized particle search–locate algorithm for arbitrary grids». In: *Journal of Computational Physics* 132.2 (1997), pp. 157–166 (cit. on pp. 22, 23).

[28] Jay P Boris. «Relativistic plasma simulation-optimization of a hybrid code». In: *Proc. Fourth Conf. Num. Sim. Plasmas*. 1970, pp. 3–67 (cit. on p. 23).

[29] Charles K Birdsall and A Bruce Langdon. *Plasma physics via computer simulation*. CRC press, 2004 (cit. on p. 24).

[30] «The Electrostatic Particle In Cell (ES-PIC) Method». In: (). URL: `https://www.particleincell.com/2010/es-pic-method/` (cit. on p. 24).

[31] FI Parra, E Ahedo, JM Fife, and M Martinez-Sanchez. «A two-dimensional hybrid model of the Hall thruster discharge». In: *Journal of Applied Physics* 100.2 (2006), p. 023304 (cit. on pp. 24, 25, 29).

[32] John R Brophy. «Stationary plasma thruster evaluation in Russia». In: (1992) (cit. on p. 28).

[33] Richard Hofer, Ioannis Mikellides, Ira Katz, and Dan Goebel. «Wall sheath and electron mobility modeling in hybrid-PIC Hall thruster simulations». In: *43rd AIAA/ASME/SAE/ASEE Joint Propulsion Conference & Exhibit*. 2007, p. 5267 (cit. on pp. 29, 39, 42, 44, 45, 48).

[34] Milo B. «Particle-In-Cell Simulation of Ions and Neutrals in Hall Effect Thruster Plasma». MA thesis. Università degli studi di Napoli, Federico II, 2020 (cit. on p. 29).

[35] Manuel Gamero-Castano and Ira Katz. «Estimation of Hall thruster erosion using HPHall». In: (2005) (cit. on p. 37).

[36] «IEPC Summer 2021 Virtual Event». In: (). URL: `https://www.iepcboston.org/summer-2021` (cit. on p. 55).

[37] «AIDAA XXVI International Congress». In: (). URL: https://aidaa2021.it/#programme (cit. on p. 55).

Ringraziamenti

Desidero ringraziare il professor Lorenzo Casalino, relatore di questa tesi, per il supporto offertomi durante questi mesi e gli ingegneri Mario Panelli e Francesco Battista per avermi dato l'opportunità di svolgere questo lavoro di tesi in collaborazione con il CIRA. Un ringraziamento speciale va a Mario che mi ha guidato in questo percorso, aiutandomi a superare "l'inferno" della numerica, e che ha contribuito alla mia crescita sia dal punto di vista tecnico che da quello umano.